



HAL
open science

Heat Balance in the Nordic Seas in a Global 1/12° Coupled Model

Anne Marie Treguier, Pierre Mathiot, Tim Graham, Dan Copsey, Camille Lique, Jean Sterlin

► **To cite this version:**

Anne Marie Treguier, Pierre Mathiot, Tim Graham, Dan Copsey, Camille Lique, et al.. Heat Balance in the Nordic Seas in a Global 1/12° Coupled Model. *Journal of Climate*, 2021, 34 (1), pp.89-106. 10.1175/JCLI-D-20-0063.1 . hal-03381862

HAL Id: hal-03381862

<https://hal.science/hal-03381862v1>

Submitted on 18 Oct 2021

HAL is a multi-disciplinary open access archive for the deposit and dissemination of scientific research documents, whether they are published or not. The documents may come from teaching and research institutions in France or abroad, or from public or private research centers.

L'archive ouverte pluridisciplinaire **HAL**, est destinée au dépôt et à la diffusion de documents scientifiques de niveau recherche, publiés ou non, émanant des établissements d'enseignement et de recherche français ou étrangers, des laboratoires publics ou privés.

ABSTRACT

14 The Nordic Seas are a gateway to the Arctic Ocean, where Atlantic water undergoes a strong
15 cooling during its transit. Here we investigate the heat balance of these regions in the high
16 resolution Met Office Global Coupled Model GC3 with a $1/12^\circ$ grid. The GC3 model reproduces
17 the contrasted ice conditions and ocean heat loss between the eastern and western regions of the
18 Nordic Seas. In the west (Greenland and Iceland seas), the heat loss experienced by the ocean is
19 stronger than the atmospheric heat gain, because of the cooling by ice melt. The latter is a major
20 contribution to the heat loss over the path of the East Greenland Current and west of Svalbard.
21 In the model, surface fluxes balance the convergence of heat in each of the eastern and western
22 regions. The net east-west heat exchange, integrated from Fram Strait to Iceland, is relatively
23 small: the westward heat transport of the Return Atlantic Current over Knipovich Ridge balances
24 the eastward heat transport by the East Icelandic Current. Time fluctuations, including eddies, are
25 a significant contribution to the net heat transports. The eddy flux represents about 20% of the total
26 heat transport in Denmark Strait and across Knipovich Ridge. The coupled ocean-atmosphere-ice
27 model may overestimate the heat imported from the Atlantic and exported to the Arctic by 10 or
28 15%. This confirms the tendency toward higher northward heat transports as model resolution is
29 refined, which will impact scenarios of future climate.

30 **1. Introduction**

31 Situated between the Greenland-Scotland Ridge and Fram Strait, the Nordic Seas are the gateway
32 between the North Atlantic and the Arctic (Fig. 1). This region of the world ocean is of considerable
33 importance because of its role in driving the Atlantic Meridional Overturning Circulation (AMOC).
34 It is established that the overflows over the Greenland-Scotland Ridge and the entrainment just
35 downstream of the sills account for at least two thirds of the dense branch of the AMOC (12 Sv,
36 Quadfasel and Käse 2007), and recent transport measurements confirm that view (Lozier et al.
37 2019; Chafik and Rossby 2019). These overflows are fed by waters of Arctic and Atlantic origin that
38 have been transformed in the Nordic Seas by interior mixing and by exchanges with the atmosphere.
39 Regarding the Arctic watermass transformations, the Nordic Seas play a preconditioning role by
40 cooling the warm Atlantic waters before they enter the Arctic ocean through Fram Strait and the
41 Barents Sea (Moat et al. 2014). The heat transport of these Atlantic waters has a strong impact
42 on Arctic basin properties (Polyakov et al. 2017; Barton et al. 2018) and Arctic climate (Docquier
43 et al. 2019), and it has been demonstrated to be a source of predictability on interannual to decadal
44 time scales in the Nordic and Barents seas in CMIP5 models (Langehaug et al. 2017).

45 There is a sharp contrast between the Norwegian Sea in the east and the Greenland and Iceland
46 seas in the west. Water of Atlantic origin circulates in the Norwegian Sea, where the heat loss to
47 the atmosphere is large. The Greenland and Iceland seas are fed by the cold waters of the East
48 Greenland Current entering through Fram Strait, and they are partly covered by sea ice in winter.
49 The complexity and variability of the ice conditions make it very difficult to quantify air-sea fluxes
50 over the area. Moreover, ice-ocean fluxes that impact water mass properties are not observable
51 directly. Although the entrance and exits of the Nordic Seas have been monitored for decades
52 (Dickson et al. 2008), the exchanges between the eastern and western part, across the Arctic front,

53 are not well known. Two eastward flowing currents have been described: the Jan Mayen Current,
54 at the latitude of the Jan Mayen island (Bourke et al. 1992) and the East Icelandic Current, north
55 of Iceland (Jónsson 2007). A westward recirculation branch, the Return Atlantic Current (Bourke
56 et al. 1988), is found at the latitudes of Fram Strait and may be eddy driven (Hattermann et al. 2016).
57 In a pioneering paper, Segtnan et al. (2011) constructed a full heat balance of the Nordic Seas from
58 observations. They compared the heat convergence into individual basins with the atmospheric
59 heat loss from reanalyses, and concluded that a significant export of heat from the Norwegian Sea
60 into the Greenland and Iceland seas was necessary to close the budget. However the observations
61 were not dense enough in space and time to infer the nature (mean flow or eddies) and the location
62 of this heat export. Recently, Asbjørnsen et al. (2019) computed the heat budget in the Norwegian
63 Sea using the ECCOv4 ocean reanalysis. They analyzed the sources of interannual variability, and
64 concluded that ocean advection was the main driver of heat content variability, the surface fluxes
65 being less important, but their study was limited to the Atlantic water domain south of 75°N.

66 In this paper, we take advantage of a new global coupled ocean-atmosphere-ice model to study
67 the full depth heat balance of the Nordic Seas and the exchanges of heat between the different
68 subbasins. This global model (Hewitt et al. 2016) has an unprecedented fine resolution of 1/12°
69 in the ocean, comparable to the state of the art regional models used to investigate the circulation
70 in the Nordic Seas. Previous studies at high resolution have mainly used ocean models forced
71 by an observed atmospheric state, rather than coupled models. A recent example is Ypma et al.
72 (2019), who estimate Atlantic water fluxes through Denmark strait in two global ocean models at
73 1/10°. Despite being forced by the same CORE dataset, these models have very contrasted sea
74 ice concentrations in the Nordic Seas, and both differ from observations. In such forced models,
75 one may question the validity of air-sea fluxes, because of the mismatch between observed air
76 temperature and modelled sea surface temperature where observed and modelled ice concentrations

77 differ (Griffies et al. 2009). In coupled models in contrast, exchanges between the ocean, ice and
78 atmosphere are fully consistent, which is an advantage for a study of the heat budget, provided that
79 the coupled model has a stable climate under constant external forcing. This is the case for the
80 GC3 model in our region of interest.

81 The paper is organized as follows. After a presentation of the model characteristics, the surface
82 properties and mass transports are compared with observations in section 3, and the heat budget
83 of the Nordic Seas is presented in section 4. We show how the full-depth convergence of heat is
84 balanced by the exchanges with the atmosphere and sea ice at the surface in the different subbasins
85 of the Nordic Seas, we quantify for the first time the east-west exchanges, and we assess the role
86 of eddies in driving the heat transports. Finally, we document the interannual variability of the
87 east-west transports within the Nordic Seas over the period of the simulation (30 years).

88 **2. Model description**

89 The Earth System Model used in this study is based on the Met Office Global Coupled 3.0
90 (GC3) configuration (Williams et al. 2018), incorporating the Global Atmosphere 7 (GA7) and the
91 Global Land 7 (GL7) configurations (Walters et al. 2019), the Global Ocean 6 (GO6) configuration
92 (Storkey et al. 2018) and the Global Sea Ice configuration (Ridley et al. 2018). The atmospheric
93 model has 85 levels on the vertical and a N512 horizontal grid (15 km over the Nordic Seas). The
94 ocean model is based on the NEMO modelling platform in geopotential coordinate with 75 levels
95 (1m resolution at the surface) on the global tri-polar grid eORCA12 (1/12° nominal resolution, i.e.
96 a 4.7 km averaged resolution in the Nordic Seas). The sea-ice model is based on the version 5.2.1
97 of the CICE base code (Hunke et al. 2015), setup with 5 ice thickness categories, 4 ice layers and
98 1 snow layer. The coupling between the ocean/ice component and the atmosphere component is
99 done with OASIS3-MCT (Craig et al. 2017) at a frequency of 1 hour. All the results described

100 here are based on a present-day climate experiment. This is a 50 year free-running simulation
101 with constant forcing values from year 2000 (solar forcing, aerosols, ozone and greenhouse gas
102 concentrations). The experiment is initialized as follows. The atmosphere initial state comes from
103 a one-year simulation of a GC3 N512-eORCA025 (global ocean at 1/4°) with forcing from year
104 2000. The ocean temperature and salinity are initialised from a climatology based on the EN4
105 objective analysis (Good et al. 2013), for the period 1995-2014. This period is long enough to
106 define a climatological state and it includes the year 2000, which has been chosen for the external
107 forcing. The ocean model is spun up from rest. The sea-ice initial condition is a snapshot from an
108 eORCA12 G06 simulation forced by atmospheric data.

109 GC3 is a pre-CMIP6 model version. Extensive validation of the GC3 N512-O012 was not
110 published. A previous version of a Global Coupled configuration (GC2.1) has been evaluated at
111 such resolution in the atmosphere and the ocean by Hewitt et al. (2016). Relative to GC2, the
112 main changes in GC3 are a new aerosol scheme, new multilayer snow scheme on land, multilayer
113 sea ice scheme and several parametrization changes in the cloud, the radiation and the convection
114 component. For CMIP6, the version GC3.1 has been built starting from GC3.0 with the inclusion
115 of a representation of spectral dispersion in the calculation of the cloud droplet effective radius
116 following Liu et al. (2008), followed by further tuning of the sea ice. The differences between
117 GC3.0 and GC3.1 are relatively small and, except for the Southern Ocean, have localised impact
118 (Williams et al. 2018). A GC3.1 N512/O012 configuration had been assessed and evaluated against
119 lower resolution configuration as part of the HighResMIP exercise and results are described in detail
120 in Roberts et al. (2019). In the present study, the last 30 years of the GC3 simulation are used
121 and the model is evaluated in the Nordic Seas using atmospheric reanalyses, a climatology of
122 surface currents from drifters (Laurindo et al. 2017), as well as satellite observations of sea surface

123 temperature (Reynolds et al. 2007) and ice concentration from NSIDC, National Snow and Ice
124 Data Center (Cavalieri et al. 1996).

125 Besides the model prognostic variables (velocity and tracers), products of temperature and
126 velocity are computed online during the simulation at each time step, averaged monthly and stored
127 on the native model grid. It is thus possible to compute heat fluxes taking into account the eddy
128 variability at all time scales, by subtracting the flux due to the time-mean flow from the total (see
129 section 4c). The calculation of transports and tracer fluxes across sections is performed following
130 staggered model grid lines, for consistency with the discretized volume conservation equation (see
131 Fig.1 of Deshayes et al. 2014, for an illustration). The domains in which flux convergence and
132 surface forcings are integrated are bounded by these staggered sections or by land grid points.

133 **3. Simulated surface properties and transports**

134 The coupled model evaluation is focussed on key aspects relevant to ocean heat transport and
135 heat exchange with the atmosphere. We consider sea surface temperature and ice concentration
136 because of their strong influence on air-sea fluxes. The realism of the volume transports through
137 key sections is also assessed, as a prerequisite to the computation of heat transports.

138 *a. Sea ice concentration, temperature and eddy kinetic energy*

139 The Greenland and Iceland seas are characterized by the large extent of their seasonal sea ice.
140 Fig. 2 shows the contrast in ice concentration between March and September climatologies of the
141 coupled model. Two isolines of sea ice concentration, 0.15 and 0.85, are outlined in gray for the
142 model and red for the observations. In March, the maximum extent of pack ice (ice concentration
143 > 0.85) is well represented by the model along the Greenland coast, but the Marginal Ice Zone
144 (MIZ), with concentrations between 0.15 and 0.85, is too wide. On the contrary, the model

145 underestimates the sea ice in Fram Strait and north of Svalbard (Fig. 2a). In September when the
146 ice is minimum (Fig. 2b), the model ice concentration agrees remarkably well with observations in
147 the Greenland Sea, but it is still underestimated north of Svalbard. Regarding the Greenland Sea,
148 Hewitt et al. (2016) also found an overestimation of sea ice with a pattern similar to Fig. 2 (their
149 Fig. 6), which was worse with the $1/4^\circ$ ocean compared with the $1/12^\circ$ version.

150 For a more quantitative comparison, we show in Fig. 3 the ice area over the region from 45°W
151 to 20°E and 65°N to 80°N . It is the sum, over the region, of the area of each cell multiplied
152 by the fractional concentration for that cell. The interannual variability is large in both models
153 and observations, with standard deviations of $5.6 \times 10^4 \text{ km}^2$ and $8.8 \times 10^4 \text{ km}^2$ respectively, which
154 explains some features of the time-mean shown in Fig. 2. When the observed ice concentration
155 is high in winter, a protrusion of the MIZ called the Odden extends over much of the Norwegian
156 Sea. Such was the case for example in 1987 and 1997 (Germe et al. 2011). Observations show
157 that the Odden has declined since the 1990s (Germe et al. 2011), which means that this feature
158 has a small footprint on the 1991-2010 average. The modelled MIZ is too extended compared
159 with the observed one (white and red contours in Fig. 2, left panel) because the model develops
160 an Odden-like feature too often, almost every year. Overall, the coupled model shows a realistic
161 seasonal cycle (Fig. 3), albeit with an amplitude larger than observed, related to the overestimation
162 of the Odden. Considering the trends over the 1985-2015 period, a decline of sea ice is observed
163 (Fig. 3a), especially in the Iceland Sea according to Våge et al. (2018). The model shows interannual
164 variability but no trend (Fig. 3b), which is expected because the external forcings (anthropogenic
165 and volcanic) are held constant.

166 The coupled model reproduces the contrasted sea surface temperature distribution of the Nordic
167 Seas (Fig. 4a), with warm temperatures along the Norwegian coast and cold temperatures in the
168 Greenland and Iceland seas in the regions partially covered by sea ice. Fig. 4b highlights some

169 regions with significant differences between the model and observations. The model SST is slightly
170 too cold in the ice-covered area of the Greenland and Iceland seas, which is consistent with the
171 large extent of the MIZ in GC3. A cold bias ($> 2^\circ$) is also found in the Lofoten and Norwegian
172 basins; it seems to be a common feature of the GC2 and GC3.1 coupled simulations analyzed by
173 Hewitt et al. (2016) and Roberts et al. (2019). Wekerle et al. (2017) found a similar bias in the
174 finite element FESOM model at 24 km resolution, forced by CORE (their Fig. 4), but in another
175 FESOM simulation at higher resolution (4.5km), the cold bias was greatly reduced. Such a bias
176 does not appear in the 4 km resolution ROMS simulation of Trodahl and Isachsen (2018); note that
177 our SST map in Fig. 4a is directly comparable to their Fig. 2.

178 Considering that eddies detached from the Norwegian Atlantic Slope Current (NwASC) transport
179 heat into the Lofoten basin (Isachsen et al. 2012; Dugstad et al. 2019), could the cold bias in GC3
180 be related to a lack of eddy activity? Fig. 5 shows that the eddy energy resulting from the NwASC
181 instabilities is realistic close to the continental slope but underestimated in the western part of the
182 Lofoten basin, compared to observations by drifters. This eddy energy pattern in CG3 is similar
183 to the ROMS model at 4 km resolution of Isachsen et al. (2012) (their Fig. 4) and Trodahl and
184 Isachsen (2018) (their Fig 2), as well as to the 4.5 km model of Wekerle et al. (2017) (their Fig.15),
185 consistent with GC3 having a similar resolution (4.7 km on average in the Nordic Seas). Clearly
186 the resolution of GC3 is not yet sufficient to represent the westward drift of eddies into the Lofoten
187 basin, and their interaction with the Lofoten Vortex, a quasi-permanent anticyclonic eddy with a
188 diameter of 18 km (Søiland et al. 2016).

189 The cold bias in GC3 does not result only from the lack of eddies, but also from an underestimation
190 of the mean advection of warm water by the offshore branch of the Norwegian Atlantic Current,
191 the Norwegian Atlantic Front Current (NwAFC). Repeated observations at the Svinøy section
192 near 63° N have been used to quantify the two branches of the Norwegian Current (Orvik et al.

193 2001). These authors suggest that the NwAFC transports 3.4 Sv of Atlantic water saltier than
194 35 psu, an amount similar to the NwASC (4.2 Sv). Mork and Skagseth (2010), using altimetry
195 and hydrography, found a much lower transport of Atlantic Water by the NwAFC (1.7 Sv), but on
196 the contrary Høydalsvik et al. (2013) suggest that the front transport is even larger than the slope
197 branch (6.8 Sv). GC3 has a weak offshore NwAFC branch carrying only 1.3 Sv of Atlantic water
198 ($S > 35$ psu) and the NwASC slope branch, inshore of the 1000 m isobath, is much stronger (5 Sv).
199 Despite the lack of agreement between different observational studies, we believe that this weak
200 NwAFC branch is a deficiency of our model, with consequences on the properties in the Lofoten
201 basin farther north. Fig. 6 compares the temperature in the model and in the climatology for the
202 month of June, along the Gimsøy section (which is outlined on the map of SST, Fig. 4a). A clear
203 temperature front is observed across Mohn Ridge (Fig. 6b), similar to synoptic plots of the section
204 (see Gascard and Mork 2008, their Fig 6.2). This front is the signature of the warm NwAFC
205 flowing northward on the eastern flank of the ridge (Fig.1). In the GC3 model (Fig. 6a), the front is
206 replaced by a weaker gradient from Mohn Ridge to Norway, hence the waters colder than observed
207 at the surface (Fig. 4b) and also at depth. This underestimation of the NwAFC in the model may
208 be due to a combination of numerical schemes and the representation of bathymetry, both of which
209 have been shown to affect mean current pathways (Barnier et al. 2006). The topographic constraint
210 may be too large in GC3, compared with other models such as FESOM (Wekerle et al. 2017) or
211 ROMS (Trodahl and Isachsen 2018), and force both branches of the Norwegian Atlantic Current
212 to merge to a large extent and to follow the slope.

213 *b. Barotropic transports*

214 To examine further the contrast between the eastern and western parts of the Nordic Seas, we have
215 computed the transports into these regions as well as the exchanges between them. The eastern

216 and western regions are delimited by sections following the bathymetric features that separate the
217 deep basins, as in Segtnan et al. (2011). In the western region we have added an additional section
218 between Greenland and the island of Jan Mayen, so that the Greenland and Iceland seas can also
219 be considered separately for some diagnostics. The sections are outlined in Fig. 7 as well as the
220 time-mean barotropic transport through each of them (red numbers and arrows). The section at
221 Fram Strait follows the 79°N latitude, and the boundary between the western and eastern part of this
222 section corresponds to the maximum southward barotropic transport cumulated from Greenland.

223 Let us consider the eastern region. In the Norwegian Sea, the water enters from the Atlantic
224 ocean over the sills and from the Greenland and Iceland seas in the west, and exits to the Barents Sea
225 and to the Arctic via Fram Strait, with also a recirculation to the Greenland Sea above Knipovich
226 Ridge. Regarding the sills, 3.9 Sv of light water cross the Iceland Faroe Ridge in the model, within
227 the uncertainty of Rossby et al. (2018)'s estimate (4.46 ± 0.7 Sv). This flow being the origin of
228 the NwAFC, the weakness of this current branch in the model is thus not a source problem but
229 rather related to processes inside the Norwegian Sea as mentioned in section 3a. The light water
230 flux between Faroe and Norway (3.2 Sv) is in agreement with the long term measurements of
231 Sherwin et al. (2008) and the synthesis of Chafik and Rossby (2019). The dense overflow in Faroe
232 Bank channel (3.1 Sv) is higher than the estimate of 2.2 Sv by Chafik and Rossby (2019), but
233 the total amount of dense water outflow east of Iceland in the model is closer to the observations
234 (2.6 Sv, Østerhus et al. 2019). Moving north along the Atlantic water path, one notes that the model
235 transport into the Barents Sea is large (3.1 Sv) compared with the 2 Sv estimated by Smedsrud et al.
236 (2010), but the outflow by the Spitzbergen Current in Fram Strait is consistent with observations
237 (Beszczynska-Möller et al. 2012). The Return Atlantic Current, south of Fram Strait, carries 1.8 Sv
238 into the Greenland Sea. This recirculation has been referred to as the Knipovich branch by Aksenov
239 et al. (2010), who computed a transport of 1.2 Sv in their numerical model. de Steur et al. (2014)

240 inferred from currentmeter arrays a recirculation of 3 Sv within 10° latitude south of 79°N. Based
241 on a synoptic acoustic current meter survey of the EGC, Håvik et al. (2017) find that the Return
242 Atlantic Current contributes 1.6 Sv to the EGC. Overall, the amplitude of this circulation in GC3,
243 1.8 Sv, seems thus fairly realistic.

244 Let us consider now the western region (Greenland and Iceland seas). The East Greenland
245 Current (EGC) carries water through Fram Strait southward, at the rate of 6.9 Sv. Probably
246 because of its high resolution, GC3 has a stronger exchange flow through Fram Strait than the
247 ocean-ice components of climate models analyzed by Ilicak et al. (2016), and more comparable
248 with the inverse estimate of 5.85 Sv by Tsubouchi et al. (2012). The transport entering the Nordic
249 Seas through Fram Strait in the coupled model is in very good agreement with the observations
250 reported by Beszczynska-Möller et al. (2012). Marnela et al. (2016) recently obtained a higher
251 transport (11 ± 3 Sv) by summing together all the observed southward flow branches through Fram
252 Strait. The model equivalent is 9.5 Sv, within the range of uncertainty of Marnela et al. (2016).

253 Mohn Ridge act as a barrier for most of the eastward transport of the Greenland Sea gyre: the
254 export of 2.1 Sv across this ridge is relatively small, compared with the total transport of the gyre
255 (see Fig. 8 and the discussion hereafter). In the Greenland Sea, more water (2.1 Sv) is exported
256 across Mohn Ridge than the amount imported across Knipovich Ridge (1.8 Sv). This unbalance
257 in water export between the two ridges results in a decrease in the total mass transport along
258 Greenland of 0.3 Sv, between the latitudes of Fram Strait and the island of Jan Mayen. Moving
259 southward into the Iceland Sea, a transport of 6.6 Sv enters between Greenland and Jan Mayen;
260 half of it exits to the North Atlantic through Denmark Strait (3.2 Sv) and half to the Norwegian
261 Sea (3.4 Sv). This latter transport, between Iceland and Jan Mayen, is difficult to validate from
262 observations. The model seems coherent with the circulation diagram of Jónsson (2007), who

263 measure 2.5 Sv in the East Icelandic Current and note that their section does not capture all the
264 eastward flow north of Iceland.

265 The total barotropic transport through Denmark strait is also difficult to validate from observa-
266 tions, because of the lack of transport measurements over the continental shelf. Østerhus et al.
267 (2019) estimate a net transport of 4.3 Sv, higher than the transport of 3.2 Sv in GC3. This net
268 transport is the result of the exchanges of light and dense waters above the Greenland-Scotland sills,
269 which are the main driver of the AMOC. To compare these inflows and outflows with observations,
270 we have computed the transport for densities above and below $\sigma_0 = 27.8$ (blue and black numbers
271 and arrows in Fig. 7). The overflow of dense water in Denmark Strait, 2.4 Sv in GC3, is indeed
272 lower than observed. Jochumsen et al. (2012), Harden et al. (2016) and Østerhus et al. (2019)
273 estimate it at 3.4 Sv, 3.54 Sv and 3.2 Sv, respectively. Averaged across the strait, the light water
274 flows to the South (0.8 Sv), but this net transport is the sum of a southward flow along Greenland
275 and a northward flow along Iceland. The northward flow of Atlantic water is 1 Sv, in agreement
276 with the observed transport of the North Icelandic Irminger Current (Østerhus et al. 2019).

277 As a result of mass conservation in the model, the net balances in the east and west regions are
278 very small compared to the transports through sections shown in Fig. 7. In the western region
279 (Greenland and Iceland seas) there is a divergence of -0.055 Sv. Most of this liquid water export
280 is caused by sea ice melt. Indeed, sea ice is advected into the region through Fram Strait, and only
281 partially exported through Denmark Strait, providing a net volume convergence of 0.035 Sv. More
282 precisely, the ice convergence in the western region results from the ice inflow at Fram (0.053
283 Sv, or 1672 km³/year, consistent with the recent estimate of Ricker et al. (2018)), which is not
284 compensated by the smaller ice export through Denmark Strait (0.017 Sv, 534 km³/year). The ice
285 exchange between the western and eastern regions is negligible, one order of magnitude smaller
286 (0.001 Sv). After taking into account the ice melt, the remaining volume divergence is 0.02 and

287 0.016 Sv in the western and eastern regions, respectively; it is forced by the input of water due to
288 the precipitation-evaporation balance and the river runoff.

289 The transport of the Greenland Sea gyre does not appear in Fig. 7 because the gyre lies entirely
290 within the boundaries of the Greenland Sea region (Fig. 8). This gyre is quite strong in the
291 coupled model, with a maximum barotropic streamfunction of 17.6 Sv at its center (computed by
292 integrating the meridional transports eastward from Greenland). In Fig.8, streamfunction values
293 of -1 to -11 are contoured in black, to show the location of the barotropic exchanges between the
294 Greenland-Iceland and Norwegian seas in relation with the subregion boundaries, and thus provide
295 a detailed information that complements Fig. 7. Inside the Greenland sea gyre, the Knipovich and
296 Mohn Ridge sections as defined do not coincide exactly with a streamfunction contour, hence a
297 local recirculation of about 2 Sv across them. However, the main fluxes exchanged between the
298 Greenland and the Norwegian seas across these two ridges are clearly located north of Knipovich
299 Ridge (the Return Atlantic Current branch) and at the southern tip of Mohn Ridge, north of Jan
300 Mayen. The flow between Jan Mayen and Iceland is concentrated in the southern part of the Iceland
301 sea, in the East Icelandic Current.

302 Fig. 7 provides a synthetic view of the full depth water transports at the entrance and exit of the
303 Nordic Seas that, to our knowledge, has never been derived from a model analysis. Indeed, most
304 modelling studies focus on specific water masses or straits, for example the Atlantic water (Aksenov
305 et al. 2010), the water exchange across Denmark strait (Ypma et al. 2019), or the transports into the
306 Arctic through Fram and the Barents Sea opening (van der Linden et al. 2019). The quantification
307 of the exchange between the Iceland and the Norwegian Seas is also new; only the East Icelandic
308 Current has been observed (Jónsson 2007) but not the flow over the Jan Mayen Ridge. In the next
309 section, we consider the heat transports associated with these volume transports and their role in
310 the heat balance of the Nordic Seas.

311 **4. Heat balance of the Nordic Seas**

312 *a. Surface ocean cooling in reanalyses and in the coupled model*

313 In theory, heat fluxes at the ocean surface give us valuable information on the processes that
314 govern the cooling and densification of surface waters in the Nordic Seas. Unfortunately, these
315 fluxes are not easy to infer from observations, and one must turn to atmospheric reanalyses. Segtnan
316 et al. (2011) used surface fluxes from two reanalysis products, ERA40 and NCEP2 for their study
317 of the Nordic Seas heat balance. They found that the total heat loss for the 1990-1999 period over
318 the Nordic Seas (excluding the Barents Sea) was 126 TW in ERA40 and 10% higher in NCEP2.
319 Here we take advantage of the ERA5 reanalysis at higher resolution to map the spatial and seasonal
320 variability of surface fluxes, and compare it with the air-sea flux computed by the coupled model. In
321 both reanalyses and model, the net atmospheric heat flux is the sum of the shortwave and longwave
322 radiative fluxes, the sensible and latent heat fluxes. Fluxes are computed using bulk formulae and
323 albedos that are different over ocean and ice. The net heat fluxes over partially covered grid cells
324 are a combination of both, weighted by the ice concentration (for more details about CG3, see
325 Hewitt et al. 2011).

326 Fig. 9a,b displays the surface heat flux for the months of March and September, and Table 1
327 presents the fluxes integrated over the western and eastern parts of the Nordic Seas (regions defined
328 by Segtnan et al. (2011) and outlined in Fig. 7). Ice concentration has its extrema in March and
329 September, but not the heat flux; for this reason the annual mean heat flux is not always comprised
330 between the March and September values. The cooling (atmospheric heat gain) in ERA5 for the
331 decade 2001-2010 is 132 TW. It occurs mainly in the eastern part of the Nordic Seas (about 2/3
332 in the east and 1/3 in the west, very similar to Segtnan et al. (2011)). The annual cycle is strong;
333 the cooling in March is about twice the annual mean (note the two different colorscales for March

334 and September in Fig. 9). In the east, the cooling extends from the Norwegian coast well into
335 the Norwegian Sea, and is the strongest along Svalbard. In the Western part of the Nordic Seas,
336 the cooling occurs mainly along the path of the EGC, along the continental slope. In winter, this
337 cooling region is located in the marginal sea ice zone. In September it occurs at the same location,
338 although the ice boundary has moved north. Therefore it appears that this flux is related to the
339 advection by the EGC, more than to the vicinity of the sea ice edge.

340 The surface flux from ERA5 is the exchange of heat with the ocean or sea ice at the base of the
341 atmosphere, that can be compared with the surface flux computed in the atmospheric component
342 of GC3 (Fig. 9b,c). Overall, the agreement is quite good. The heat loss in the center of the
343 Norwegian Sea is underestimated in the model, which is certainly related to the cold bias (Fig. 4).
344 This confirms that the cold SST in the Norwegian Sea results from a bias in the ocean circulation
345 rather than an excessive atmospheric cooling.

346 With the coupled model we can estimate directly the heat flux at the ocean surface, below
347 the sea ice (Fig. 9e,f). The ocean experiences a strong heat loss along the path of the EGC. In
348 fact, the ocean surface cooling integrated in the western region is stronger (more negative) than
349 the warming experienced by the atmosphere (Table 1). This difference between the ocean and
350 atmosphere surface fluxes in the coupled model must be due, in part, to ice melting. There is a
351 net ice melt in the Greenland Sea in the annual average, because the advection of ice from the
352 Arctic is larger than the ice export through Denmark Strait, as mentioned in the previous section
353 (a convergence of 0.035 Sv, corresponding to a cooling of 10.6 Tw). The cooling due to ice melt
354 is also in part responsible for the strong heat loss just north of Fram Strait off Svalbard in the
355 model (Fig. 9e,f), larger than suggested by ERA5. The model heat loss may be overestimated in
356 this region; this could be related to the high sea surface temperature of the water flowing along
357 Svalbard and entering the Arctic as shown in Fig. 4. A complete analysis of the difference between

358 the heat fluxes seen by the ocean and by the atmosphere would require all the components of the
359 sea ice heat budget, but some terms are not available in the model output files.

360 *b. Full-depth heat convergence in the coupled model*

361 We compute in the ocean model the total convergence of heat into the two regions, as well as the
362 contributions of mean flow and time fluctuations to this convergence (Table 2). The convergence of
363 heat in the western and eastern region is consistent with the surface heat fluxes, although a residual
364 of 5 TW indicates a warming trend in the Nordic Seas in the model, over the 30 years considered.
365 This trend is concentrated in the Norwegian Sea (an equivalent surface flux of 3.7 W.m^{-2}). As
366 the coupled simulation used constant anthropogenic forcings corresponding to the year 2000,
367 it is difficult to conclude whether this trend is a decadal variability simulated by the model, a
368 drift resulting from imperfect model numerics and parameterizations, or whether it results from
369 a discrepancy between the coupled model forcing and its initial conditions. Observations in the
370 Norwegian basin between 2011 and 2018 (Mork et al. 2019) show a warming of 0.046°C per year
371 in the upper 1000 m, corresponding to a surface flux of 6.3 W.m^{-2} , due to the combination of
372 anthropogenic warming and internal variability. Broomé et al. (2020), using ocean heat content
373 over the Atlantic Water area in the Norwegian Sea, find a warming equivalent to 5 W.m^{-2} over the
374 period 1993-2002 but no warming between 2004 and 2013 . The heat imbalance in the coupled
375 model is thus of a magnitude that does not exceed observed decadal trends and it is not larger than
376 drifts and trends found in forced ocean model simulations.

377 Besides the heat convergence, Table 2 also lists the heat transports across individual sections.
378 The mass transport being non zero, these numbers depend on the reference temperature. We have
379 chosen 0°C , as in Segtnan et al. (2011) and in almost all estimates from observations (e.g., Østerhus
380 et al. 2005). A regional picture of the full-depth heat balance is provided in Fig. 10. Almost 300 TW

381 of heat enters the Nordic Seas over the sills between Greenland and Norway. About half of it is
382 lost to the atmosphere or sea ice (Table 1), and the other half enters the Arctic through the Barents
383 Sea and the Spitzbergen Current. Considering the Norwegian Sea only, 261 TW of heat enters
384 over the Iceland-Scotland Ridge, and the ratio of heat loss processes is about $2/3$ of Arctic export
385 and only $1/3$ of atmospheric loss. In addition to the exchanges with the Atlantic and Arctic oceans,
386 Fig. 10 displays the east-west fluxes inside the Nordic Seas, and quantifies them in an integrated
387 perspective. The model shows 24 TW of heat entering the Greenland Sea over the Knipovich
388 and Mohn ridges, contributing to balance the surface heat loss over the Greenland Sea, which is
389 30.3 TW. In the southern part of the domain, a similar amount of heat (26 TW) is exported from the
390 Iceland Sea into the Norwegian Sea. This export is necessary because the surface heat loss over the
391 Iceland Sea (16.5 TW) does not balance the heat input through Denmark Strait. Integrated from
392 Fram Strait all the way to Iceland, the sum of the east-west exchanges is relatively small (2 TW).
393 Thus, the model gives a consistent picture of the heat balance in the Norwegian Sea with almost no
394 net heat export to the Greenland and Iceland seas, the exchanges with these two seas compensating
395 each other.

396 This contrasts with Segtnan et al. (2011), who attempted to construct the heat balance of the
397 western and eastern part of the Nordic Seas by estimating the convergence of heat from observations.
398 They found that the total heat convergence in the eastern region (Norwegian Sea), 119 TW, was
399 higher than the surface heat loss by 35 TW, but that the heat convergence in the western region
400 was lower than the surface heat loss by about 36 TW. They concluded that a heat flux from the
401 Norwegian Sea into the Greenland and Iceland seas was probably necessary to close the heat
402 budget, but they could not estimate this exchange due to a lack of data. The difficulty to build a
403 heat balance from observations stems from the fact that most in situ measurements focus on an
404 individual water mass, for example the so-called "Atlantic water" (AW). Studies based on these

405 observations use definitions of this water mass that differ from one section to the next, making it
406 impossible to infer robust regional balances from the published literature. We emphasize that in a
407 numerical model, full-depth heat transport calculations such as displayed in Fig. 10 seem the best
408 way to present a consistent heat budget of the Nordic Seas.

409 Is the budget realistic in the coupled model? Model-observations comparisons can be made by
410 calculating a model proxy for the observations; note that in the following, the model transports are
411 not the full depth values of Table 2 but rather AW transports, each computed with the same method
412 as in the observational reference cited. Three branches of AW entering the Nordic Seas have been
413 monitored (Østerhus et al. 2005). The model-data agreement is excellent for the Shetland branch:
414 112 TW in GC3 vs. 107 TW in Berx et al. (2013). The AW model transport in the Faroe branch,
415 measured along a section north of the Faroes, is high: 151 TW in GC3 vs 124 ± 15 TW computed
416 by Hansen et al. (2015). Finally, the Iceland branch in Denmark Strait seems also overestimated
417 in the model: 33 TW in GC3 vs. 24 TW in Jónsson and Valdimarsson (2012). Thus, there may be
418 an excess of heat entering the Nordic Seas in GC3: the full-depth heat transport from Greenland
419 to Norway, 299 TW, is indeed larger than the 273 Tw estimated by Chafik and Rossby (2019). The
420 excess of heat in the model is not released to the atmosphere and seems to result in larger than
421 observed outflows to the Arctic. Both exit routes have stronger heat transport than observed: the
422 Barents Sea opening with 91 TW vs. 70 TW in Smedsrud et al. (2013), as well as Fram Strait with
423 59 TW in GC3 vs. 40 TW in Schauer et al. (2008). This large heat transport from the Atlantic to the
424 Arctic may be related to the high resolution of GC3. Indeed in the CORE model intercomparison
425 Ilicak et al. (2016) found that the model with the highest resolution had the highest heat transports,
426 a finding supported by the comparison of CMIP5 models by Heuzé and Årthun (2019).

427 Let us add a note of caution regarding the east-west heat exchange in the model. If one considers
428 the volume fluxes west of Fram Strait (6.9 Sv, Fig. 7) and at Denmark Strait (3.2 Sv) as reasonable,

429 this means that a compensating eastward volume flux of about 3.7 Sv exists between Fram strait and
 430 Iceland. In the model the total transport of the eastward flowing branches is even higher (5.5 Sv),
 431 to compensate for the westward RAC (-1.8 Sv). The latitudinal distribution of these eastward
 432 currents may be affected by the model weak NwAFC along Mohn Ridge. For example, the 2.1 Sv
 433 crossing Mohn Ridge in Fig. 7 could be overestimated and the flow between Jan Mayen and Iceland
 434 correspondingly underestimated. Furthermore, the east-west volume transport being nonzero, the
 435 associated heat transports depend on the temperature reference. The heat transport across Mohn
 436 Ridge in Fig. 10 is opposite to the volume transport because there are negative temperatures over the
 437 ridge; it would change sign if the freezing temperature of seawater had been chosen as a reference
 438 instead of zero.

439 *c. Eddy and seasonal contribution to the time-mean heat fluxes*

440 The coupled model gives us access to the heat transports due to temporal fluctuations, that is,
 441 the correlations of velocity and temperature that can result in a time-mean transport. Let us define
 442 v as the velocity normal to a section, T the temperature, the time-average by an overbar and the
 443 departures from the time-average by primes, and integrate over depth and the length of a section s :

$$\iint_s \overline{vT} = \iint_s \bar{v}\bar{T} + \iint_s \overline{v'T'} \quad (1)$$

444 The $\overline{v'T'}$ correlations occur at all time scales. Table 2 presents separately the heat transport by
 445 the time-mean flow and the transients, the latter being further decomposed into a seasonal and an
 446 eddy part. The transient seasonal contribution is defined as the difference between the averaged
 447 heat transport of 12 monthly means (the monthly climatology being computed over 30 years) and
 448 the heat transport by the 30-year time-mean flow. Overall, the seasonal contribution is smaller than
 449 the eddy one. This means that the correlation of the velocity and temperature on seasonal cycles

450 do not contribute much to the total heat transport, despite the large seasonal variability across most
451 sections. For example, the model reproduces the amplification of the recirculation over Knipovich
452 Ridge in winter and spring by a factor of two (Hattermann et al. 2016), and the large seasonal
453 cycle of the Atlantic water transport by the Spitzbergen Current in Fram Strait (also a factor of two
454 between summer and winter, in agreement with Beszczynska-Möller et al. 2012).

455 Let us consider now the transient eddy heat flux. The eddy heat convergence (Table 2) is
456 remarkably large in the Greenland and Iceland seas, where it represents 23% of the total heat
457 convergence (10.7 TW). It is much smaller in proportion in the Norwegian Sea, 2% of the total.
458 There are two hotspots of eddy heat transport into the Greenland and Iceland seas (Table 2). One
459 is over Knipovich Ridge, with an eddy flux of 4.1 TW, more than 18% of the total. The second is
460 across Denmark Strait, with an eddy contribution of 7.7 TW representing 20% of the total transport.
461 These strong eddy fluxes are plausible, because the presence of eddies has been documented in the
462 recirculation south of Fram Strait (Hattermann et al. 2016) as well as in Denmark Strait (Appen
463 et al. 2017). The eddy heat fluxes across the Iceland-Faroe Ridge and the Barents Sea opening are
464 also large in magnitude (8.1 TW and 5.9 TW, respectively) but they represent a lower proportion
465 of the total heat transport which is large through these sections (146 TW and 94 TW respectively).

466 **5. Interannual variability of heat exchanges between the Greenland-Iceland and Norwegian** 467 **seas**

468 Understanding the variability of heat transport from the North Atlantic into the Arctic is crucial
469 in the context of Arctic climate change. This variability has been investigated in a large number
470 of numerical models. In coupled models the North Atlantic heat transport has been shown to be
471 anticorrelated with the volume of sea ice in the Arctic ocean (Docquier et al. 2019). Årthun and
472 Eldevik (2016) analyzed a 500-years long simulation of the low resolution coupled Bergen Climate

473 Model and found that the heat entering the Norwegian Sea was a source of predictability for the
474 Arctic temperature with a time lag of 14 years. More recently, Muilwijk et al. (2018) analyzed the
475 variability in a century-long forced simulation of the same model. de Boer et al. (2018) studied
476 the variability of volume transports through Arctic straits and their correlations using both a $1/3^\circ$
477 and a $1/12^\circ$ coupled model similar to GC3. The ongoing HighResMip experiments (Roberts et al.
478 2019) will provide new opportunities to investigate the multidecadal variability of the AW inflow
479 into the Arctic. Here, we use the relatively short GC3 experiment to document the interannual
480 variability. We focus on the east-west exchanges within the Nordic Seas, because they are expected
481 to contribute to the variability of the pathways into the Arctic, and they are poorly documented.

482 We have computed time series of the annual mean volume and heat transports mapped in Figs. 7
483 and 10 and found no large trends in the 30-years series (selected time series are shown in Figs. 11 to
484 13). Standard deviations based on annual means (*std*) are within the range of the CORE-II models
485 (Ilicak et al. 2016) for the main pathways into the Arctic. For example, in the Barents Sea Opening
486 (BSO) the *std* of volume transport in GC3 is 0.34 Sv (0.32 to 0.65 for the CORE-II models) and
487 the *std* of heat transport is 10.2 TW (5.6 to 13.6 in CORE-II). Correlations between sections are
488 presented in Table 3; unless indicated, all correlations reported in this paper are significant at the
489 95% level (p-value < 0.05).

490 In Fram Strait, there is a strong anticorrelation (-0.9) between the southward EGC branch along
491 Greenland (Fram W) and the northward Spitzbergen Current branch along Svalbard (Fram E), an
492 anticorrelation that was also found in a different model by Muilwijk et al. (2018). The *std* of volume
493 transport is thus larger for each individual branch (0.81 and 0.87 Sv) than for the total flow through
494 Fram Strait (0.45 Sv, consistent with Schauer et al. 2008). Interestingly, the heat transports of the
495 two branches are also anticorrelated, but less strongly so than their volume transports (-0.4). This
496 anticorrelation may be due to a recirculation of AW north of 79° N. As expected, the variability of

497 the total heat transport through Fram Strait is dominated by the eastern branch carrying warm AW
498 (correlation of 0.96). The *std* of the total heat transport through Fram Strait, 10.6 TW, is larger
499 than the one found in the CORE-II models, reflecting the stronger and more realistic exchange flow
500 in GC3 compared with lower resolution models. At the southern entrance of the Nordic Seas, the
501 volume transports on both sides of Iceland are strongly anticorrelated (-0.7 between the Denmark
502 and Icl-Norw sections, Table 3). This is expected, because both these transports are affected by the
503 same atmospheric variability (Sorterberg et al. 2005), but it does not result in a similar correlation
504 for the heat transport through these sections. There is also a correlation between the volume
505 transport at the entrance of the Nordic Seas and Fram Strait, as suggested by de Boer et al. (2018).

506 We focus now on the east-west exchanges. First, we consider the interannual variability of
507 the recirculation over Knipovich Ridge, compared with the branches that exit the Norwegian Sea
508 through Fram Strait and the BSO (Fig. 11). As expected, there is a correlation (0.5) between the
509 volume transport exiting through Fram Strait (Fram E) and the volume flowing westward over
510 Knipovich Ridge. In absolute values this is an anticorrelation: when more volume follows the
511 Spitzbergen Current, less recirculates south of Fram Strait, and vice-versa. However this relationship
512 does not hold for the transport of heat. The heat transports across the Fram east section and across
513 Knipovich Ridge tend to co-vary, indicating a stronger influence of temperature variability than
514 volume transport. Note, however, that the positive correlation of heat transports suggested by
515 Fig. 11 is not significant. There is also no significant correlation between the volume transport
516 exiting through BSO and the Fram east section, contrary to Muilwijk et al. (2018) who found a
517 high correlation in their low resolution model. One possible explanation is the presence of eddies
518 in GC3, which may contribute to decorrelate the transports at the interannual time scale. This is
519 in agreement with de Boer et al. (2018) who found a correlation of -0.9 between the total Fram
520 and BSO transports in a low resolution model, but only -0.5 in the high resolution case; and also

521 with Asbjørnsen et al. (2019)'s conclusion that eddy parameterizations have a dampening effect on
522 interannual variability of heat fluxes. The correlation is similar in CG3 (-0.4; see Table 3). Unlike
523 the volume transports, the heat transports through Fram East and BSO are correlated positively at
524 lag zero (0.4), indicating that temperature anomalies can affect both sections the same year.

525 The variability of the four inflows and outflows of the Greenland Sea is represented in Fig. 12.
526 The *std* of the heat flux over Knipovich Ridge (6.7 TW) is about twice as large as the three other
527 sections. In contrast, for the volume flux the EGC (Fram W section) is the branch with the
528 largest variability. The volume flux entering over Knipovich Ridge and exiting over Mohn Ridge
529 are similar (1.8 and 2.1 Sv), as well as their standard deviations (0.59 and 0.66 Sv), but these
530 two branches are not connected by a simple loop. Indeed, the Mohn Ridge volume flux is not
531 correlated with the Knipovich Ridge flux at the interannual time scale, while it has significant
532 correlations with the Fram West and Jan Mayen-Greenland transports (0.5 and 0.4, respectively,
533 Table 3). The absence of correlation between the circulations over Knipovich and Mohn ridges
534 is consistent with Håvik et al. (2017), who observed that a significant part of the warm water
535 carried by the recirculation south of Fram Strait enters the EGC and can then be entrained into the
536 Greenland gyre circulation or carried along the Greenland slope into the Iceland Sea. The heat
537 transports in GC3 are consistent with the circulation pattern observed by Håvik et al. (2017), with
538 a strong correlation (0.6) between the heat transport anomalies over Knipovich Ridge and across
539 the Jan Mayen-Greenland section (appearing as an anticorrelation in Fig. 12 because of the sign
540 convention).

541 Let us finally consider the Iceland Sea (Fig. 13). The EGC inflow between Jan Mayen island
542 and Greenland does not show any significant correlation with the Denmark strait section. On the
543 other hand, the transport between Jan Mayen and Iceland is correlated with both the EGC and
544 Denmark Strait transports. For volume transport the correlation is strongest with the Jan Mayen-

545 Greenland branch (-0.7) than with the Denmark strait branch (0.4); for heat transport, the opposite
546 is true and there is a strong correlation between heat transport anomalies through Denmark strait
547 and between Jan Mayen and Iceland (0.7), probably due to the variability of the East Icelandic
548 Current which connects these two sections. Finally, eastward transports north and south of Jan
549 Mayen are anticorrelated (-0.6 correlation between Mohn and Jmay-Icl, Table 3): a strong transport
550 over Mohn Ridge means less transport south of Jan Mayen and vice versa. However despite this
551 relationship between volume transports, there is no correlation of the heat transports carried by
552 these two branches at the interannual time scales.

553 In summary, the 30-years time series of transports between the Norwegian Sea and the Greenland-
554 Iceland seas shows that the variability of east-west transports at interannual time scales is compa-
555 rable to the variability of the exchanges with the Atlantic or the Arctic. Two branches play a key
556 role by carrying relatively warm waters of Atlantic origin between the eastern and western basins:
557 the recirculation over Knipovich Ridge south of Fram Strait, and the East Icelandic Current. The
558 coupled model suggests that the variability of the Knipovich branch drives part of the variability
559 of the EGC heat transport between Greenland and the island of Jan Mayen.

560 **6. Conclusions**

561 In this study we have used a global, fully coupled atmosphere-land-ocean-sea ice model to
562 investigate the regional dynamics of the Nordic Seas. This is made possible by the high resolution
563 of the GC3 simulation, which has been found to improve a number of key ocean circulation
564 processes (Hewitt et al. 2016, 2017). For example, de Boer et al. (2018) noted that the 1/12° model
565 had a more realistic transport through the Canadian Archipelago than a lower resolution climate
566 model. In the Nordic Seas, the integrated sea ice area is much closer to observations in GC3 than
567 in the three coupled climate models investigated by Langehaug et al. (2017). Additionally the heat

568 transport into the Nordic Seas is very well represented, compared with the climate models evaluated
569 by Heuzé and Årthun (2019). For regional analyses such as ours, model simulations forced by a
570 prescribed atmospheric state are often preferred to fully coupled models; recent examples at high
571 resolution are Aksenov et al. (2010); Wekerle et al. (2017); Schlichtholz et al. (2019); Ypma et al.
572 (2019). Before choosing the CG3 coupled simulation, we compared it with a simulation of the
573 same $1/12^\circ$ ice-ocean model forced by CORE atmospheric forcings, and found that biases were
574 similar in both the coupled and the forced simulations (not shown). We found that the forced model
575 overestimates the ice concentration (similar to Fig. 2) and displays SST biases (similar to Fig. 4).
576 For our investigation of the heat balance we have chosen the coupled model because it has fully
577 consistent ocean-ice-atmosphere fluxes, contrary to forced models which may have spurious fluxes
578 where the simulated ice distribution does not match the observed one (Griffies et al. 2009).

579 We have taken advantage of the high resolution of the model (4.7 km) to compute a full-depth
580 heat budget separately for different subregions of the Nordic Seas. By considering the ocean heat
581 budget under the sea-ice, we highlight the importance of cooling due to ice melt in the Greenland
582 and Iceland seas. This cooling is concentrated along the path of the EGC as well as west of
583 Svalbard. The model conserves mass and does not have any large drift of its heat content, a
584 necessary condition to compute full-depth volume and heat budgets in the subregions. These
585 integrated budgets, in three separate ocean basins, are the main result of this paper (Figs. 7, 10).
586 Contrary to Segtnan et al. (2011), we do not find that a net east-west heat exchange between the
587 Norwegian Sea and the Greenland-Iceland seas is necessary to close the budget. The east-west
588 exchange of heat in the model is dominated by the recirculation over Knipovich Ridge to the north,
589 exporting heat out of the Norwegian Sea, and the East Icelandic Current to the south, bringing
590 heat into the Norwegian Sea. In the GC3 model these heat transports almost cancel each other.
591 The main discrepancy between Segtnan's estimate and ours is the heat transport through Denmark

592 Strait, which Segtnan assumes to be 5 TW to the south for liquid water. Such a southward heat
593 transport does not seem compatible with the inflow of Atlantic water along the Icelandic slope,
594 which carries 22-24 TW northward (Østerhus et al. 2005; Chafik and Rossby 2019). We thus
595 consider that the heat convergence of 46 TW in the Greenland-Iceland seas in GC3 is more realistic
596 than Segtnan's 9 TW.

597 We have estimated, for the first time, the eddy contribution to the time-mean heat transports in
598 the Nordic Seas. Eddy transports play an important role in the coupled simulation. The eddy
599 heat fluxes represent a quarter of the total heat convergence into the Greenland-Iceland seas. Eddy
600 fluxes are important over Knipovich Ridge (4.1 TW), over the Iceland-Faroe Ridge (8.1 TW),
601 through Denmark Strait (7.7 TW) and the Barent Sea opening (5.9 TW). These values may be
602 underestimated, as suggested by the comparison with drifters (Fig. 5), because of the model grid
603 resolution which is still insufficient to fully resolve eddies in weakly stratified regions where the
604 Rossby radius is small (7 km in the Norwegian Sea, Nurser and Bacon 2014) . These strong eddy
605 heat fluxes have important implications for observational strategies to measure heat transports in
606 the Nordic Seas. The eddy-generated oceanic "intrinsic" variability impacts the interannual time
607 scales (Penduff et al. 2018). Also, as eddies are generated locally, their variability may make it
608 more difficult to find spatially coherent patterns of heat anomalies propagating from the Atlantic
609 to the Arctic in high resolution models, as compared to low resolution climate models. Note that
610 even in the absence of ocean eddies, coherent surface anomalies tend to be masked by the strong
611 interannual variability of local surface fluxes (Asbjørnsen et al. 2019).

612 Despite its heat balance being as good as the one achieved in forced models in multi-decadal
613 simulations, the coupled model has some biases which may influence its performance for projections
614 of future climate. The amount of heat entering the Nordic Seas from the North Atlantic is probably
615 overestimated by 10-15%. The excess heat is not released to the atmosphere but rather enters

616 the Arctic ocean, where it could potentially affect the sea ice cover and trigger climate feedbacks.
617 The heat loss may be underestimated in GC3 in the Norwegian Sea due to the weakness of the
618 Norwegian Atlantic Front Current. Our findings are consistent with the general pattern of large
619 heat transports in the Atlantic and into the Arctic at high resolution (Roberts et al. 2019). Docquier
620 et al. (2019) also found that coupled models at a resolution of $1/4^\circ$ tend to have a higher Atlantic
621 heat transport and, consequently, a lower Arctic sea ice than coarser resolution models. Such a
622 dependency of the meridional heat transport in the Atlantic on ocean grid resolution is well known.
623 It has been first demonstrated in ocean models forced by a prescribed atmosphere (e.g., Hecht and
624 Smith 2008; Treguier et al. 2012). Forced ocean model experiments, such as defined by the Ocean
625 Model Intercomparison Project (Griffies et al. 2016) will thus be useful to develop and validate
626 future high resolution coupled models for climate.

627 *Data availability statement.* The GC3 model data are available via the CEDA-JASMIN platform,
628 upon request to the MetOffice authors.

629 *Acknowledgments.* We thank Pascale L’Herminier for sharing her views of the circulation of the
630 Nordic Seas and drafting Figure 1. Anne Marie Treguier is supported by CNRS, and Camille
631 Lique by Ifremer. Pierre Mathiot and Tim Graham are supported by the Met Office Hadley Centre
632 Climate Programme funded by BEIS and Defra (GA01101). We acknowledge extensive use of
633 the supercomputers at the Met Office and the ARCHER UK National Supercomputing Service to
634 complete the simulations and the CEDA-JASMIN platform for enabling data storage and model
635 analysis. The authors acknowledge the JWCRP Joint Marine Modelling Programme for providing
636 support and access to model configurations and output.

References

- Aksenov, Y., S. Bacon, A. C. Coward, and A. G. Nurser, 2010: The north Atlantic inflow to the Arctic Ocean: High-resolution model study. *Journal of Marine Systems*, **79 (1)**, 1 – 22, doi:<https://doi.org/10.1016/j.jmarsys.2009.05.003>.
- Appen, W.-J. v., D. Mastropole, R. S. Pickart, H. Valdimarsson, S. Jónsson, and J. B. Girton, 2017: On the nature of the mesoscale variability in Denmark Strait. *Journal of Physical Oceanography*, **47 (3)**, 567–582, doi:10.1175/JPO-D-16-0127.1.
- Årthun, M., and T. Eldevik, 2016: On anomalous ocean heat transport toward the Arctic and associated climate predictability. *Journal of Climate*, **29 (2)**, 689–704, doi:10.1175/JCLI-D-15-0448.1.
- Asbjørnsen, H., M. Arthun, O. Skagseth, and T. Eldevik, 2019: Mechanisms of ocean heat anomalies in the norwegian sea. *Journal of Geophysical Research: Oceans*, **124 (4)**, 2908–2923, doi:10.1029/2018JC014649, URL <https://agupubs.onlinelibrary.wiley.com/doi/abs/10.1029/2018JC014649>, <https://agupubs.onlinelibrary.wiley.com/doi/pdf/10.1029/2018JC014649>.
- Barnier, B., and Coauthors, 2006: Impact of partial steps and momentum advection schemes in a global ocean circulation model at eddy-permitting resolution. *Ocean Dynamics*, **56 (5-6)**, 543–567.
- Barton, B. I., Y.-D. Lenn, and C. Lique, 2018: Observed atlantification of the Barents Sea causes the polar front to limit the expansion of winter sea ice. *Journal of Physical Oceanography*, **48 (8)**, 1849–1866, doi:10.1175/JPO-D-18-0003.1.
- Berx, B., B. Hansen, S. Østerhus, K. M. Larsen, T. Sherwin, and K. Jochumsen, 2013: Combining in situ measurements and altimetry to estimate volume, heat and salt transport variability through the Faroe-Shetland Channel. *Ocean Science*, **9 (4)**, 639–654, doi:10.5194/os-9-639-2013.

659 Beszczynska-Möller, A., E. Fahrbach, U. Schauer, and E. Hansen, 2012: Variability in Atlantic
660 water temperature and transport at the entrance to the Arctic Ocean, 1997-2010. *ICES Journal*
661 *of Marine Science*, **69 (5)**, 852–863, doi:10.1093/icesjms/fss056.

662 Bourke, R. H., R. G. Paquette, and R. F. Blythe, 1992: The Jan Mayen Current of the Greenland
663 Sea. *Journal of Geophysical Research: Oceans*, **97 (C5)**, 7241–7250, doi:10.1029/92JC00150.

664 Bourke, R. H., A. M. Weigel, and R. G. Paquette, 1988: The westward turning branch of the West
665 Spitsbergen Current. *Journal of Geophysical Research: Oceans*, **93 (C11)**, 14 065–14 077,
666 doi:10.1029/JC093iC11p14065.

667 Broomé, S., L. Chafik, and J. Nilsson, 2020: Mechanisms of decadal changes in sea surface
668 height and heat content in the eastern nordic seas. *Ocean Science*, **16 (3)**, 715–728, doi:10.5194/
669 os-16-715-2020, URL <https://os.copernicus.org/articles/16/715/2020/>.

670 Cavalieri, D. J., C. L. Parkinson, P. Gloersen, and H. J. Zwally, 1996: Sea ice concentrations
671 from Nimbus-7 SMMR and DMSP SSM/I-SSMIS Passive Microwave Data. NASA National
672 Snow and Ice Data Center Distributed Active Archive Center, Boulder, Colorado USA, doi:
673 <https://doi.org/10.5067/8GQ8LZQVL0VL>.

674 Chafik, L., and T. Rossby, 2019: Volume, heat, and freshwater divergences in the subpolar north
675 atlantic suggest the nordic seas as key to the state of the meridional overturning circulation.
676 *Geophysical Research Letters*, **46 (9)**, 4799–4808, doi:10.1029/2019GL082110, URL <https://agupubs.onlinelibrary.wiley.com/doi/abs/10.1029/2019GL082110>.

677

678 Craig, A., S. Valcke, and L. Coquart, 2017: Development and performance of a new version of
679 the OASIS coupler, OASIS3-MCT_3.0. *Geoscientific Model Development*, **10 (9)**, 3297–3308,
680 doi:10.5194/gmd-10-3297-2017.

681 de Boer, A. M., E. Gavilan Pascual-Ahuir, D. P. Stevens, L. Chafik, D. K. Hutchinson, Q. Zhang,
682 L. C. Sime, and A. J. Willmott, 2018: Interconnectivity between volume transports through
683 arctic straits. *Journal of Geophysical Research: Oceans*, **123** (12), 8714–8729, doi:10.1029/
684 2018JC014320, URL <https://agupubs.onlinelibrary.wiley.com/doi/abs/10.1029/2018JC014320>.

685 de Steur, L., E. Hansen, C. Mauritzen, A. Beszczynska-Möller, and E. Fahrbach, 2014: Im-
686 pact of recirculation on the east greenland current in fram strait: Results from moored
687 current meter measurements between 1997 and 2009. *Deep Sea Research Part I: Oceanographic Research Papers*, **92**, 26 – 40, doi:<https://doi.org/10.1016/j.dsr.2014.05.018>, URL
688 <http://www.sciencedirect.com/science/article/pii/S0967063714001009>.

689

690 Deshayes, J., R. Curry, and R. Msadek, 2014: CMIP5 Model Intercomparison of Freshwater
691 Budget and Circulation in the North Atlantic. *Journal of Climate*, **27** (9), 3298–3317, doi:
692 10.1175/JCLI-D-12-00700.1, URL <https://doi.org/10.1175/JCLI-D-12-00700.1>.

693 Dickson, R., J. Meincke, and P. Rhines, Eds., 2008: *Arctic-Subarctic Ocean Fluxes: Defining the*
694 *Role of the Northern Seas in Climate*. Springer, Dordrecht.

695 Docquier, D., and Coauthors, 2019: Impact of model resolution on arctic sea ice and north atlantic
696 ocean heat transport. *Climate dynamics*, **53**, 4989–5017, doi:10.1007/s00382-019-04840-y.

697 Dugstad, J., I. Fer, J. LaCasce, M. Sanchez de La Lama, and M. Trodahl, 2019: Lateral heat
698 transport in the lofoten basin: Near-surface pathways and subsurface exchange. *Journal of*
699 *Geophysical Research: Oceans*, **124** (5), 2992–3006, doi:10.1029/2018JC014774.

700 Gascard, J., and K. Mork, 2008: Climatic importance of large scale and mesoscale circulation in the
701 lofoten basin deduced from lagrangian observations. *Arctic-Subarctic Ocean Fluxes*, R. Dickson,
702 J. Meincke, and P. Rhines, Eds., Springer, Dordrecht, chap. 6, 131–144.

- 703 Germe, A., M.-N. Houssais, C. Herbaut, and C. Cassou, 2011: Greenland Sea sea ice variability
704 over 1979-2007 and its link to the surface atmosphere. *Journal of Geophysical Research: Oceans*,
705 **116 (C10)**, doi:10.1029/2011JC006960.
- 706 Good, S. A., M. J. Martin, and N. A. Rayner, 2013: EN4: quality controlled ocean temperature
707 and salinity profiles and monthly objective analyses with uncertainty estimates. *Journal of*
708 *Geophysical Research: Oceans*, **118**, 6704–6716, doi:10.1002/2013JC009067.
- 709 Griffies, S. M., and Coauthors, 2009: Coordinated Ocean-ice Reference Experiments (COREs).
710 *Ocean Modelling*, **26 (1-2)**, 1–46.
- 711 Griffies, S. M., and Coauthors, 2016: OMIP contribution to CMIP6: experimental and diagnostic
712 protocol for the physical component of the Ocean Model Intercomparison Project. *Geoscientific*
713 *Model Development*, **9 (9)**, 3231–3296, doi:10.5194/gmd-9-3231-2016.
- 714 Hansen, B., K. M. H. Larsen, H. Hátún, R. Kristiansen, E. Mortensen, and S. Østerhus, 2015:
715 Transport of volume, heat, and salt towards the Arctic in the Faroe Current 1993-2013. *Ocean*
716 *Science*, **11 (5)**, 743–757, doi:10.5194/os-11-743-2015.
- 717 Harden, B., and Coauthors, 2016: Upstream sources of the denmark strait overflow: Obser-
718 vations from a high-resolution mooring array. *Deep Sea Research Part I: Oceanographic*
719 *Research Papers*, **112**, 94 – 112, doi:https://doi.org/10.1016/j.dsr.2016.02.007, URL [http:](http://www.sciencedirect.com/science/article/pii/S0967063715301266)
720 [//www.sciencedirect.com/science/article/pii/S0967063715301266](http://www.sciencedirect.com/science/article/pii/S0967063715301266).
- 721 Hattermann, T., P. E. Isachsen, W.-J. von Appen, J. Albrechtsen, and A. Sundfjord, 2016: Eddy-driven
722 recirculation of Atlantic water in Fram Strait. *Geophysical Research Letters*, **43 (7)**, 3406–3414,
723 doi:10.1002/2016GL068323.

724 Hecht, M., and R. Smith, 2008: Towards a physical understanding of the North Atlantic: a review
725 of model studies. *Ocean Modeling in an Eddy Regime*, AGU Geophysical Monography, Vol.
726 177, AGU, 213–240.

727 Heuzé, C., and M. Årthun, 2019: The Atlantic inflow across the Greenland-Scotland ridge in cli-
728 mate models (CMIP5). *Elementa Science of the Anthropocene*, **7 (1)**, 16, doi:10.1525/elementa.
729 354.

730 Hewitt, H. T., D. Copsey, I. D. Culverwell, C. M. Harris, R. S. R. Hill, A. B. Keen, A. J. McLaren,
731 and E. C. Hunke, 2011: Design and implementation of the infrastructure of hadgem3: the
732 next-generation met office climate modelling system. *Geoscientific Model Development*, **4 (2)**,
733 223–253, doi:10.5194/gmd-4-223-2011, URL <https://gmd.copernicus.org/articles/4/223/2011/>.

734 Hewitt, H. T., and Coauthors, 2016: The impact of resolving the Rossby radius at mid-latitudes
735 in the ocean: results from a high-resolution version of the Met Office GC2 coupled model.
736 *Geoscientific Model Development*, **9 (10)**, 3655–3670, doi:10.5194/gmd-9-3655-2016.

737 Hewitt, H. T., and Coauthors, 2017: Will high-resolution global ocean models benefit coupled
738 predictions on short-range to climate timescales? *Ocean Modelling*, **120**, 120–136, doi:<https://doi.org/10.1016/j.ocemod.2017.11.002>.

740 Høydalsvik, F., C. Mauritzen, K. Orvik, J. LaCasce, C. Lee, and J. Gobat, 2013: Transport
741 estimates of the western branch of the norwegian atlantic current from glider surveys. *Deep Sea*
742 *Research Part I: Oceanographic Research Papers*, **79**, 86 – 95, doi:[https://doi.org/10.1016/j.dsr.](https://doi.org/10.1016/j.dsr.2013.05.005)
743 [2013.05.005](https://doi.org/10.1016/j.dsr.2013.05.005).

744 Håvik, L., R. S. Pickart, K. Våge, D. Torres, A. M. Thurnherr, A. Beszczynska-Möller, W. Wal-
745 czowski, and W.-J. von Appen, 2017: Evolution of the East Greenland Current from Fram

746 Strait to Denmark Strait: Synoptic measurements from summer 2012. *Journal of Geophysical*
747 *Research: Oceans*, **122 (3)**, 1974–1994, doi:10.1002/2016JC012228.

748 Hunke, E., W. Lipscomb, A. K. Turner, N. Jeffery, , and S. Elliott, 2015: CICE: The Los Alamos Sea
749 Ice Model Documentation and Software User’s Manual Version 5.1. Tech. Rep. LA-CC-06-012,
750 Los Alamos National Laboratory, Los Alamos, NM, U.S.A.

751 Ilicak, M., and Coauthors, 2016: An assessment of the Arctic Ocean in a suite of interannual
752 CORE-II simulations. part III: Hydrography and fluxes. *Ocean Modelling*, **100**, 141 – 161,
753 doi:https://doi.org/10.1016/j.ocemod.2016.02.004.

754 Isachsen, P. E., I. Koszalka, and J. H. LaCasce, 2012: Observed and modeled surface eddy
755 heat fluxes in the eastern Nordic Seas. *Journal of Geophysical Research: Oceans*, **117 (C8)**,
756 doi:10.1029/2012JC007935.

757 Jochumsen, K., D. Quadfasel, H. Valdimarsson, and S. Jónsson, 2012: Variability of the Denmark
758 Strait overflow: Moored time series from 1996-2011. *Journal of Geophysical Research: Oceans*,
759 **117 (C12)**, doi:10.1029/2012JC008244.

760 Jónsson, S., 2007: Volume flux and fresh water transport associated with the East Icelandic Current.
761 *Progress in Oceanography*, **73 (3)**, 231 – 241, doi:https://doi.org/10.1016/j.pocean.2006.11.003.

762 Jónsson, S., and H. Valdimarsson, 2012: Water mass transport variability to the North Icelandic
763 shelf, 1994-2010. *ICES Journal of Marine Science*, **69 (5)**, 809–815, doi:10.1093/icesjms/fss024.

764 Langehaug, H. R., D. Matei, T. Eldevik, K. Lohmann, and Y. Gao, 2017: On model differences and
765 skill in predicting sea surface temperature in the Nordic and Barents seas. *Climate Dynamics*,
766 **48 (3)**, 913–933, doi:10.1007/s00382-016-3118-3.

- 767 Laurindo, L. C., A. J. Mariano, and R. Lumpkin, 2017: An improved near-surface velocity clima-
768 tology for the global ocean from drifter observations. *Deep Sea Research Part I: Oceanographic*
769 *Research Papers*, **124**, 73 – 92, doi:<https://doi.org/10.1016/j.dsr.2017.04.009>.
- 770 Liu, Y., P. H. Daum, H. Guo, and Y. Peng, 2008: Dispersion bias, dispersion effect,
771 and the aerosol–cloud conundrum. *Environmental Research Letters*, **3** (4), 045 021, doi:
772 [10.1088/1748-9326/3/4/045021](https://doi.org/10.1088/1748-9326/3/4/045021).
- 773 Locarnini, R. A., and Coauthors, 2018: *World Ocean Atlas 2018, Volume 1: Temperature*, Vol.
774 NOAA Atlas NESDIS 81. 52pp pp.
- 775 Lozier, M. S., and Coauthors, 2019: A sea change in our view of overturning in the subpolar North
776 Atlantic. *Science*, **363** (6426), 516–521, doi:[10.1126/science.aau6592](https://doi.org/10.1126/science.aau6592).
- 777 Marnela, M., B. Rudels, I. Goszczko, A. Beszczynska-Möller, and U. Schauer, 2016: Fram
778 Strait and Greenland Sea transports, water masses, and water mass transformations 1999-2010
779 (and beyond). *Journal of Geophysical Research: Oceans*, **121** (4), 2314–2346, doi:[10.1002/](https://doi.org/10.1002/2015JC011312)
780 [2015JC011312](https://doi.org/10.1002/2015JC011312).
- 781 Moat, B. I., S. A. Josey, and B. Sinha, 2014: Impact of Barents Sea winter air-sea exchanges
782 on Fram Strait dense water transport. *Journal of Geophysical Research: Oceans*, **119** (2),
783 1009–1021, doi:[10.1002/2013JC009220](https://doi.org/10.1002/2013JC009220).
- 784 Mork, K. A., and Ø. Skagseth, 2010: A quantitative description of the Norwegian Atlantic
785 Current by combining altimetry and hydrography. *Ocean Science*, **6** (4), 901–911, doi:[10.5194/](https://doi.org/10.5194/os-6-901-2010)
786 [os-6-901-2010](https://doi.org/10.5194/os-6-901-2010).

- 787 Mork, K. A., Ø. Skagseth, and H. Sjøiland, 2019: Recent warming and freshening of the
788 Norwegian Sea observed by Argo data. *Journal of Climate*, **32** (12), 3695–3705, doi:
789 10.1175/JCLI-D-18-0591.1.
- 790 Muilwijk, M., L. H. Smedsrud, M. Ilicak, and H. Drange, 2018: Atlantic water heat transport
791 variability in the 20th century Arctic Ocean from a global ocean model and observations.
792 *Journal of Geophysical Research: Oceans*, **123**, 8159–8179, doi:10.1029/2018JC014327.
- 793 Nurser, A. J. G., and S. Bacon, 2014: The rossby radius in the arctic ocean. *Ocean Science*, **10** (6),
794 967–975, doi:10.5194/os-10-967-2014, URL <https://os.copernicus.org/articles/10/967/2014/>.
- 795 Orvik, K. A., Ø. Skagseth, and M. Mork, 2001: Atlantic inflow to the Nordic Seas: current structure
796 and volume fluxes from moored current meters, VM-ADCP and SeaSoar-CTD observations,
797 1995–1999. *Deep Sea Research Part I: Oceanographic Research Papers*, **48** (4), 937 – 957,
798 doi:[https://doi.org/10.1016/S0967-0637\(00\)00038-8](https://doi.org/10.1016/S0967-0637(00)00038-8).
- 799 Østerhus, S., W. R. Turrell, S. Jonsson, and B. Hansen, 2005: Measured volume, heat, and salt
800 fluxes from the Atlantic to the Arctic Mediterranean. *Geophysical Research Letters*, **32** (7),
801 doi:10.1029/2004GL022188.
- 802 Østerhus, S., and Coauthors, 2019: Arctic Mediterranean exchanges: a consistent volume budget
803 and trends in transports from two decades of observations. *Ocean Science*, **15** (2), 379–399,
804 doi:10.5194/os-15-379-2019.
- 805 Penduff, T., and Coauthors, 2018: Chaotic variability of ocean heat content: Climate-relevant
806 features and observational implications. *Oceanography*, **31**.
- 807 Polyakov, I. V., and Coauthors, 2017: Greater role for Atlantic inflows on sea-ice loss in the Eurasian
808 Basin of the Arctic Ocean. *Science*, **356** (6335), 285–291, doi:10.1126/science.aai8204.

- 809 Quadfasel, D., and R. Käse, 2007: Present-day manifestation of the Nordic Seas overflows. *Ocean*
810 *Circulation: Mechanisms and Impacts* Past and Future Changes of Meridional Overturning,
811 A. Schmittner, J. Chaing, and S. Hemming, Eds., American Geophysical Union (AGU), chap.
812 3.1, 75–89, doi:10.1029/173GM07.
- 813 Reynolds, R. W., T. Smith, C. Liu, D. Chelton, K. Casey, and M. Schlax, 2007: Daily high-
814 resolution-blended analyses for sea surface temperature. *J. Climate*, **20**, 5473–5496.
- 815 Ricker, R., F. Girard-Ardhuin, T. Krumpen, and C. Lique, 2018: Satellite-derived sea ice export
816 and its impact on Arctic ice mass balance. *The Cryosphere*, **12** (9), 3017–3032, doi:10.5194/
817 tc-12-3017-2018.
- 818 Ridley, J. K., E. W. Blockley, A. B. Keen, J. G. L. Rae, A. E. West, and D. Schroeder, 2018:
819 The sea ice model component of HadGEM3-GC3.1. *Geoscientific Model Development*, **11** (2),
820 713–723, doi:10.5194/gmd-11-713-2018.
- 821 Roberts, M. J., and Coauthors, 2019: Description of the resolution hierarchy of the global coupled
822 HadGEM3-GC3.1 model as used in CMIP6 HighResMIP experiments. *Geoscientific Model*
823 *Development*, **12** (12), 4999–5028, doi:10.5194/gmd-12-4999-2019.
- 824 Rossby, T., C. Flagg, L. Chafik, B. Harden, and H. Sjøiland, 2018: A direct estimate of vol-
825 ume, heat, and freshwater exchange across the Greenland-Iceland-Faroe-Scotland ridge. *Jour-*
826 *nal of Geophysical Research: Oceans*, **123** (10), 7139–7153, doi:10.1029/2018JC014250,
827 URL <https://agupubs.onlinelibrary.wiley.com/doi/abs/10.1029/2018JC014250>, <https://agupubs.onlinelibrary.wiley.com/doi/pdf/10.1029/2018JC014250>.
- 828
829 Schauer, U., A. Beszczynska-Möller, W. Walczowski, E. Fahrbach, J. Piechura, and E. Hansen,
830 2008: Variation of measured heat flow through the Fram Strait between 1997 and 2006. *Arctic-*

831 *Subarctic Ocean Fluxes*, R. Dickson, J. Meincke, and P. Rhines, Eds., Springer, Dordrecht,
832 chap. 3, 65–85.

833 Schlichtholz, P., J. Marciniak, and W. Maslowski, 2019: Proxies for heat fluxes to the Arctic Ocean
834 through Fram Strait. *Ocean Modelling*, **137**, 21 – 39, doi:[https://doi.org/10.1016/j.ocemod.2019.](https://doi.org/10.1016/j.ocemod.2019.02.007)
835 02.007.

836 Segtnan, O. H., T. Furevik, and A. D. Jenkins, 2011: Heat and freshwater budgets of the Nordic
837 Seas computed from atmospheric reanalysis and ocean observations. *Journal of Geophysical*
838 *Research: Oceans*, **116 (C11)**, doi:10.1029/2011JC006939.

839 Sherwin, T., S. Hughes, W. Turrell, B. Hansen, and S. Østerhus, 2008: Wind-driven monthly
840 variations in transport and the flow field in the Faroe-Shetland Channel. *Polar Research*, **27 (1)**,
841 7–22.

842 Smedsrud, L. H., R. Ingvaldsen, J. E. Ø. Nilsen, and Ø. Skagseth, 2010: Heat in the
843 Barents Sea: transport, storage, and surface fluxes. *Ocean Science*, **6 (1)**, 219–234, doi:
844 10.5194/os-6-219-2010.

845 Smedsrud, L. H., and Coauthors, 2013: The role of the Barents sea in the Arctic climate system.
846 *Reviews of Geophysics*, **51 (3)**, 415–449, doi:10.1002/rog.20017.

847 Sjøiland, H., L. Chafik, and T. Rossby, 2016: On the long-term stability of the Iofoten basin eddy.
848 *Journal of Geophysical Research: Oceans*, **121 (7)**, 4438–4449, doi:10.1002/2016JC011726.

849 Sorterberg, A., N. G. Kvamstø, and O. Byrkjedal, 2005: Wintertime nordic seas cyclone vari-
850 ability and its impact on oceanic volume transports into the nordic seas. *The Nordic seas, an*
851 *integrated perspective*, H. Drange, T. Dokken, T. Furevik, R. Gerdes, and W. Berger., Eds., AGU,
852 Geophysical monograph 158, Washington D.C., 137–156.

- 853 Storkey, D., and Coauthors, 2018: UK Global Ocean GO6 and GO7: a traceable hier-
854 archy of model resolutions. *Geoscientific Model Development*, **11** (8), 3187–3213, doi:
855 10.5194/gmd-11-3187-2018.
- 856 Taburet, G., A. Sanchez-Roman, M. Ballarotta, M.-I. Pujol, J.-F. Legeais, F. Fournier, Y. Faugere,
857 and G. Dibarboue, 2019: Duacs dt2018: 25 years of reprocessed sea level altimetry products.
858 *Ocean Science*, **15** (5), 1207–1224, doi:10.5194/os-15-1207-2019, URL <https://os.copernicus.org/articles/15/1207/2019/>.
- 860 Treguier, A. M., J. Deshayes, C. Lique, R. Dussin, and J. M. Molines, 2012: Eddy contributions
861 to the meridional transport of salt in the North Atlantic. *J. Geophys. Res.*, **117**, C05 010.
- 862 Trodahl, M., and P. E. Isachsen, 2018: Topographic Influence on Baroclinic Instability and the
863 Mesoscale Eddy Field in the Northern North Atlantic Ocean and the Nordic Seas. *Journal*
864 *of Physical Oceanography*, **48** (11), 2593–2607, doi:10.1175/JPO-D-17-0220.1, URL <https://doi.org/10.1175/JPO-D-17-0220.1>.
- 866 Tsubouchi, T., and Coauthors, 2012: The Arctic Ocean in summer: A quasi-synoptic inverse
867 estimate of boundary fluxes and water mass transformation. *Journal of Geophysical Research*,
868 **117**, C01 024.
- 869 Våge, K., L. Papritz, L. Håvik, M. A. Spall, and G. W. K. Moore, 2018: Ocean convection
870 linked to the recent ice edge retreat along east Greenland. *Nature Communications*, **9** (1), 1287,
871 doi:10.1038/s41467-018-03468-6.
- 872 van der Linden, E. C., D. Le Bars, R. Bintanja, and W. Hazeleger, 2019: Oceanic heat transport
873 into the arctic under high and low co2 forcing. *Climate Dynamics*, **53** (7), 4763–4780, doi:
874 10.1007/s00382-019-04824-y.

- 875 Walters, D., and Coauthors, 2019: The met office unified model global atmosphere 7.0/7.1 and
876 jules global land 7.0 configurations. *Geoscientific Model Development*, **12** (5), 1909–1963,
877 doi:10.5194/gmd-12-1909-2019.
- 878 Wekerle, C., Q. Wang, W.-J. von Appen, S. Danilov, V. Schourup-Kristensen, and T. Jung, 2017:
879 Eddy-resolving simulation of the atlantic water circulation in the fram strait with focus on
880 the seasonal cycle. *Journal of Geophysical Research: Oceans*, **122** (11), 8385–8405, doi:
881 10.1002/2017JC012974.
- 882 Williams, K. D., and Coauthors, 2018: The Met Office Global Coupled Model 3.0 and 3.1 (GC3.0
883 and GC3.1) Configurations. *Journal of Advances in Modeling Earth Systems*, **10** (2), 357–380,
884 doi:10.1002/2017MS001115.
- 885 Ypma, S., N. Brüggemann, S. Georgiou, P. Spence, H. Dijkstra, J. Pietrzak, and C. Katsman,
886 2019: Pathways and watermass transformation of atlantic water entering the nordic seas through
887 denmark strait in two high resolution ocean models. *Deep Sea Research Part I: Oceanographic*
888 *Research Papers*, **145**, 59 – 72, doi:<https://doi.org/10.1016/j.dsr.2019.02.002>.

889 **LIST OF TABLES**

890 **Table 1.** Surface heat flux (TW) integrated over the western and eastern parts of the
 891 Nordic Seas (a negative value represents ocean cooling). 42

892 **Table 2.** Heat transport convergence (TW) for the western and eastern parts of the Nordic
 893 Seas in the GC3 model (a negative value represents ocean cooling). Model
 894 transports are averaged over 30 years. The total convergence is the sum of the
 895 convergence due to the time-mean flow and the convergence resulting from the
 896 time fluctuations ("Transient"). This contribution is further decomposed into
 897 a seasonal part and an "eddy" part. The heat transports through the sections
 898 outlined in Fig. 6 are also listed; the limit between the east and west sections
 899 in Fram Strait is the location of the maximum barotropic transport cumulated
 900 from Greenland. The sign convention is the following: for the eastern region,
 901 all heat transport contributions are counted positive into the region. For the
 902 budget of the western region, heat transports at Fram Strait and Denmark strait
 903 are positive into the region. The heat transports over Knipovich Ridge and from
 904 Mohn Ridge to Jan Mayen and Iceland must be counted with the opposite sign.
 905 The heat transport through Fram Strait and the Barent Sea opening are thus
 906 shown as negative, representing northward and eastward heat transports into the
 907 Arctic. 43

908 **Table 3.** Correlations between volume transports and heat transports across sections
 909 pairs, computed from 30 years of annual means in the GC3 model. In this table,
 910 all transports are counted positive eastward and northward. Correlations below
 911 95% confidence index (p value higher than 0.05) are not shown. The sections
 912 follow the pathways indicated in Fig. 7. The western, eastern and full sections
 913 are indicated for Fram Strait. BSO is the Barents Sea Opening, Knip and Mohn
 914 the sections across Knipovich and Mohn Ridges. Integrated transports between
 915 the island of Jan Mayen and Iceland and Greenland (Jmay-Icl and Jmay-Gre)
 916 are indicated, as well as transports through Denmark Strait and between Iceland
 917 and Norway (noted Denmark and Icl-Norw, respectively). 44

918 TABLE 1. Surface heat flux (TW) integrated over the western and eastern parts of the Nordic Seas (a negative
 919 value represents ocean cooling).

	Western region			Eastern region		
	Annual Mean	March	September	Annual Mean	March	September
ERA5 surface flux (1991-2010)	-39	-111	-24	-93	-188	-61
Atmosphere model surface flux	-27	-94	-30	-90	-198	-61
Ocean model surface flux	-47	-110	-42	-96	-206	-61

920 TABLE 2. Heat transport convergence (TW) for the western and eastern parts of the Nordic Seas in the GC3
921 model (a negative value represents ocean cooling). Model transports are averaged over 30 years. The total
922 convergence is the sum of the convergence due to the time-mean flow and the convergence resulting from the
923 time fluctuations ("Transient"). This contribution is further decomposed into a seasonal part and an "eddy" part.
924 The heat transports through the sections outlined in Fig. 6 are also listed; the limit between the east and west
925 sections in Fram Strait is the location of the maximum barotropic transport cumulated from Greenland. The sign
926 convention is the following: for the eastern region, all heat transport contributions are counted positive into the
927 region. For the budget of the western region, heat transports at Fram Strait and Denmark strait are positive into
928 the region. The heat transports over Knipovich Ridge and from Mohn Ridge to Jan Mayen and Iceland must
929 be counted with the opposite sign. The heat transport through Fram Strait and the Barent Sea opening are thus
930 shown as negative, representing northward and eastward heat transports into the Arctic.

Heat convergence (TW)					
extend	Total	Mean	Transient	Seasonal	Eddy
Greenland Sea	30.5	25.7	4.9	0.6	4.3
Iceland Sea	16.	10.3	5.7	-0.6	6.3
Western region	46.6	36	10.6	-0.1	10.7
Eastern region	99.8	103.6	-3.8	-2.1	-1.7

Heat transport (TW)					
	Total	Mean	Transient	Seasonal	Eddy
Fram Strait West	10.9	12.1	-1.2	-0.3	-0.9
Fram Strait East	-70.3	-69	-1.3	0.5	-1.8
Denmark Strait (DS)	37.7	29.3	8.4	0.7	7.7
Knipovich Ridge	-22.4	-17.5	-4.9	0.8	4.1
Mohn Ridge	-2.2	-1.9	-0.34	0.02	-0.36
Jan Mayen to Iceland	26.6	24.7	1.9	1.2	0.7
Barents Sea opening	-94	-85.6	-8.6	2.7	5.9
Iceland-Faroe (IFR)	146	139	8.1	0.	8.1
Faroe-Norway (FSN)	115	113	1.4	-0.3	1.7

931 TABLE 3. Correlations between volume transports and heat transports across sections pairs, computed from
932 30 years of annual means in the GC3 model. In this table, all transports are counted positive eastward and
933 northward. Correlations below 95% confidence index (p value higher than 0.05) are not shown. The sections
934 follow the pathways indicated in Fig. 7. The western, eastern and full sections are indicated for Fram Strait.
935 BSO is the Barents Sea Opening, Knip and Mohn the sections across Knipovich and Mohn Ridges. Integrated
936 transports between the island of Jan Mayen and Iceland and Greenland (Jmay-Icl and Jmay-Gre) are indicated,
937 as well as transports through Denmark Strait and between Iceland and Norway (noted Denmark and Icl-Norw,
938 respectively).

Volume	Fram W	Fram E	Fram	BSO	Knip	Mohn	Jmay-Icl	Jmay-Gre	Denmark	Icl-Norw
Fram W	1.0	–	–	–	–	–	–	–	–	–
Fram E	-0.9	1.0	–	–	–	–	–	–	–	–
Fram	0.4		1.0	–	–	–	–	–	–	–
BSO			-0.4	1.0	–	–	–	–	–	–
Knip	-0.6	0.5	-0.4		1.0	–	–	–	–	–
Mohn	-0.5		-0.5			1.0	–	–	–	–
Jmay-Icl						-0.6	1.0	–	–	–
Jmay-Gre	0.4	-0.6				0.4	-0.7	1.0	–	–
Denmark		-0.4				-0.4	0.4		1.0	–
Icl-Norw		0.4	0.5					-0.6	-0.7	1.0
Heat	Fram W	Fram E	Fram	BSO	Knip	Mohn	Jmay-Icl	Jmay-Gre	Denmark	Icl-Norw
Fram W	1.0	–	–	–	–	–	–	–	–	–
Fram E	-0.4	1.0	–	–	–	–	–	–	–	–
Fram		1.0	1.0	–	–	–	–	–	–	–
BSO		0.4	0.4	1.0	–	–	–	–	–	–
Knip					1.0	–	–	–	–	–
Mohn		-0.4	-0.4			1.0	–	–	–	–
Jmay-Icl				0.4			1.0	–	–	–
Jmay-Gre					0.6		-0.5	1.0	–	–
Denmark							0.7		1.0	–
Icl-Norw		0.7	0.6	0.6		-0.5				1.0

LIST OF FIGURES

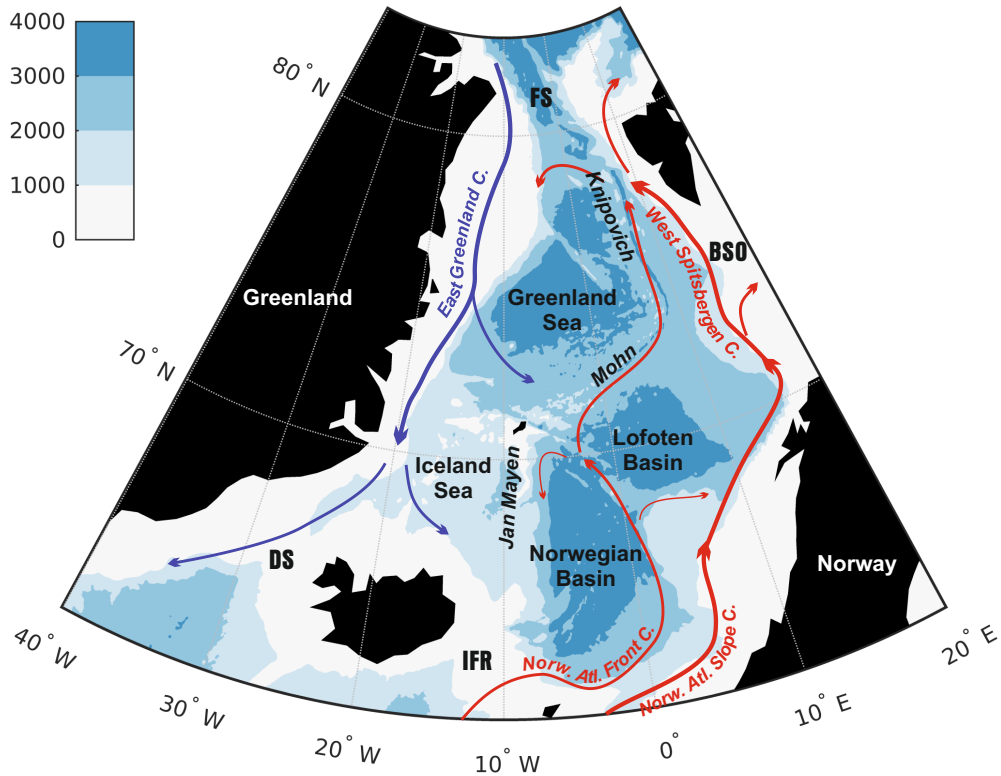
939		
940	Fig. 1.	Bathymetry of the Nordic Seas (m). The main straits allowing exchanges with the Atlantic and the Arctic are indicated: DS (Denmark Strait), IFR (Iceland Faroe Ridge), BSO (Barents Sea opening) and FS (Fram Strait), as well as the main seas (Greenland, Iceland, Norwegian seas), deep ocean ridges (Knipovich, Mohn and Jan Mayen), and the two deep basins of the Norwegian Sea (Lofoten Basin and Norwegian Basin). The bathymetric field is taken from the GC3 1/12° model. The main currents carrying Atlantic water are outlined in red (Norwegian Atlantic Slope Current, Norwegian Atlantic Front Current, West Spitzbergen Current). The East Greenland Current, carrying Arctic water, is outlined in blue. The current paths are based on Taburet et al. (2019). 47
941		
942		
943		
944		
945		
946		
947		
948		
949	Fig. 2.	Ice concentration in the coupled model, averaged over 30 years in March (left) and September (right). Grey contours indicate ice concentrations of 0.15 and 0.85. The red contours represent concentrations of 0.15 and 0.85 in NSIDC satellite observations for the same months, averaged over the 1991-2010 period. 48
950		
951		
952		
953	Fig. 3.	Ice area in the region 45°W to 20°E and 65°N to 80°N, monthly (thin lines) and annual averages (thick line). a: observations. b: coupled model. 49
954		
955	Fig. 4.	a: Sea surface temperature (°C) averaged over 20 years in the coupled model. The black line is the path of the Gimsøy section, used for Fig.6. b: difference between model SST and observed SST (averaged over years 1991-2010). 50
956		
957		
958	Fig. 5.	Left: rms surface velocity (m/s) from the GC3 coupled model. Right: rms surface velocity from a climatology of surface drifters (Laurindo et al. 2017). 51
959		
960	Fig. 6.	Climatological temperature (°C) for the month of June along the Gimsøy section, indicated on the map in Fig. 4a. a: GC3 model monthly mean, averaged over 30 years. b: monthly climatology from observations, World Ocean Atlas 2018 (Locarnini et al. 2018). The white line indicates the top of Mohn Ridge. 52
961		
962		
963		
964	Fig. 7.	Mass balance of the Nordic Seas in the coupled model. Red arrows (red numbers) represent the depth-integrated ocean mass flux (Sv) across the sections outlined in black. Short names are indicated for the sections; they are used in the tables and explained in the text (e.g, "BSO" for Barents Sea Opening). For the southern sections, the two additional numbers (blue and black) indicate the transport associated with mean densities lower and higher than $\sigma_0 = 27.8$, respectively. The sign convention is such that a positive number is a contribution in the same direction as the total indicated by the red arrow. Thin blue and black arrows indicate the direction of these light inflows and dense overflows. The grey contours represent the 500 m and 2000 m isobaths. 53
965		
966		
967		
968		
969		
970		
971		
972		
973	Fig. 8.	Barotropic streamfunction (Sv) in the coupled model, averaged over 30 years. The sections delimiting the regions of Fig. 7 are indicated in grey. Only the contours from -1 Sv to -11 Sv are outlined in black, to better show the transports entering and exiting the Greenland gyre, while keeping the readability of the figure. 54
974		
975		
976		
977	Fig. 9.	Surface heat flux climatologies for March (left panels) and September (right panels), in $W.m^{-2}$, with the limits of the Marginal sea Ice Zone (MIZ) overlaid in red (concentration 0.15 and 0.85). a,b: heat flux at the atmospheric lower boundary from ERA5 (averaged over years 2001-2010) and sea ice from NSIDC data . c, d: heat flux at the atmospheric model lower boundary, with the modelled MIZ overlaid. e, f: ocean surface heat flux and modelled MIZ. Note the different color scales for March and September. 55
978		
979		
980		
981		
982		

983 **Fig. 10.** Heat balance of the Nordic Seas in the coupled model. Red arrows represent the heat flux
984 referenced to 0°C, in units of TW, across the sections outlined in black. Values have been
985 rounded relative to the numbers in Table.2 for readability. In the Greenland Sea and in the
986 Iceland Sea the total convergence of heat, 30 TW and 16 TW respectively, balance the cooling
987 at the ocean surface within less than 1 TW. In the Norwegian Sea, the heat convergence of
988 99 TW differs from the surface heat loss (94 TW), generating a warming of 5 TW. The grey
989 contours represent the 500 m and 2000 m isobaths. 56

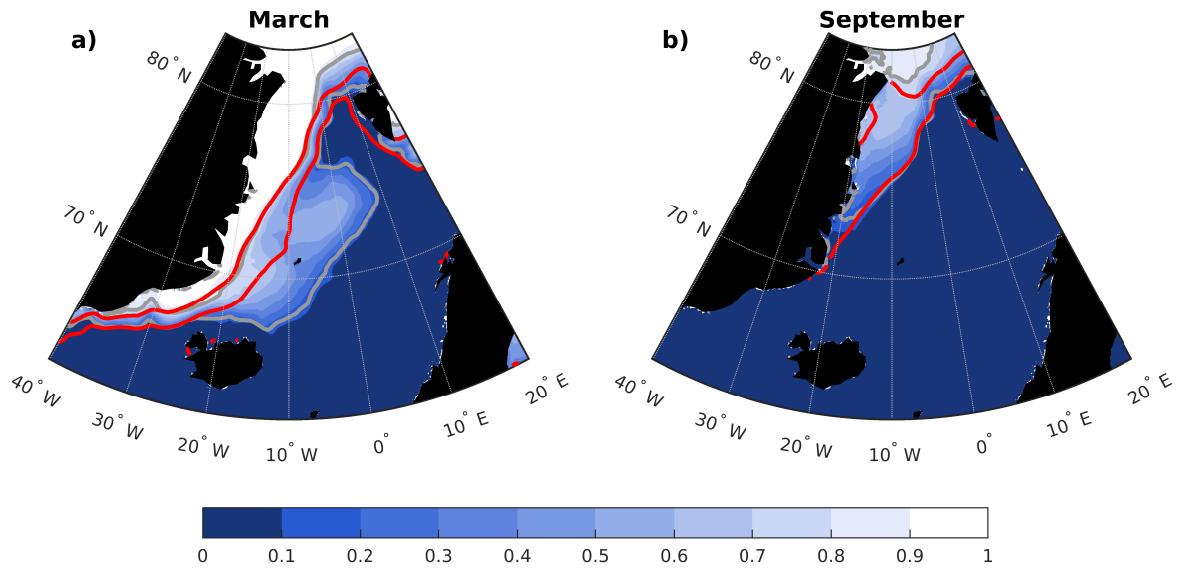
990 **Fig. 11.** Interannual anomalies of volume and heat transport across the three sections where warm
991 water exits the Norwegian Sea: Barents Sea opening (BSO), Eastern part of Fram Strait
992 (Fram E) and flow over Knipovich Ridge (Knip. R). All transports are counted positively in
993 the sense of an exit from the Norwegian Sea. The time axis is in model years. 57

994 **Fig. 12.** Interannual anomalies of volume and heat transport across the four sections enclosing the
995 Greenland Sea: Western part of Fram Strait (Fram W), flow over Knipovich Ridge (Knip.
996 R) and Mohn Ridge (Mohn R.), and between Greenland and the island of Jan Mayen. The
997 time axis is in model years. 58

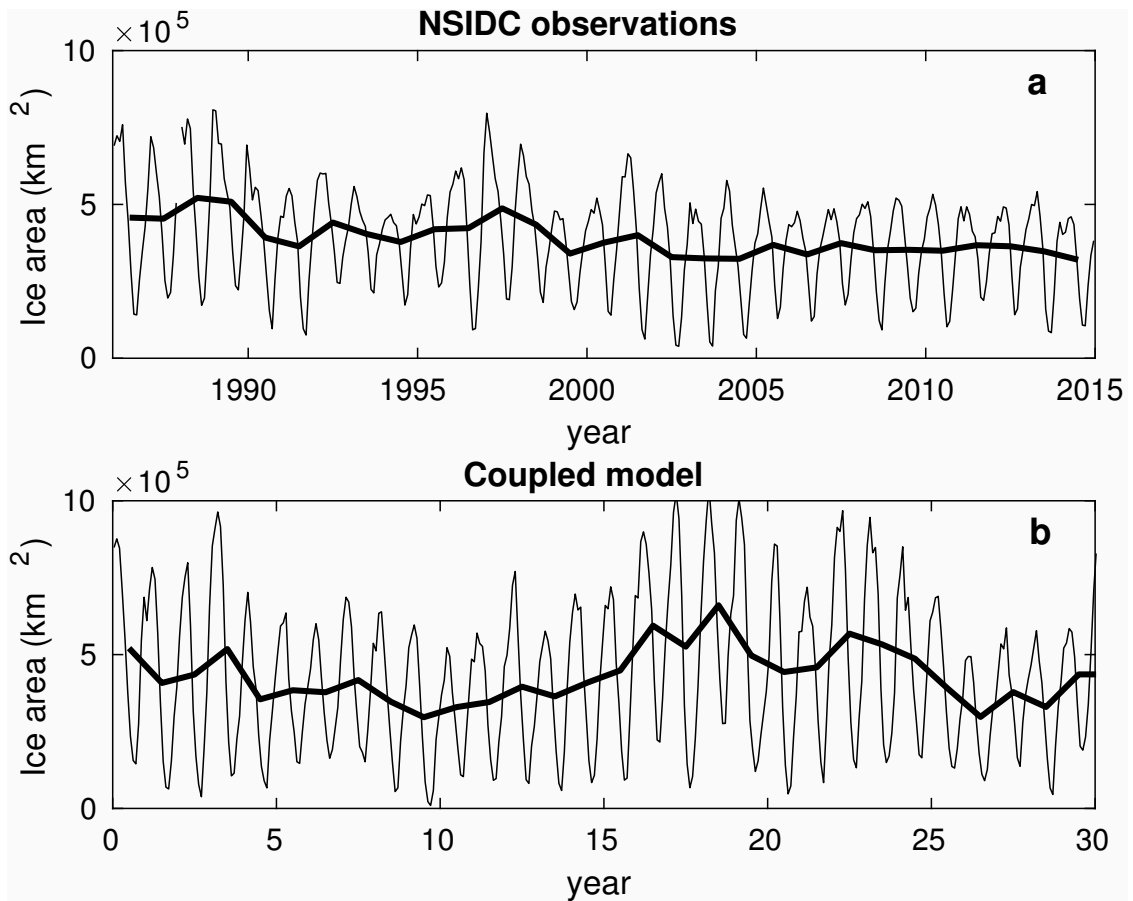
998 **Fig. 13.** Interannual anomalies of volume and heat transport across the sections enclosing the Iceland
999 Sea: Denmark Strait, flow between Greenland and Jan mayen (JanMayen) and flow between
1000 Jan Mayen and Iceland (JMay-Iceland). The time axis is in model years. 59



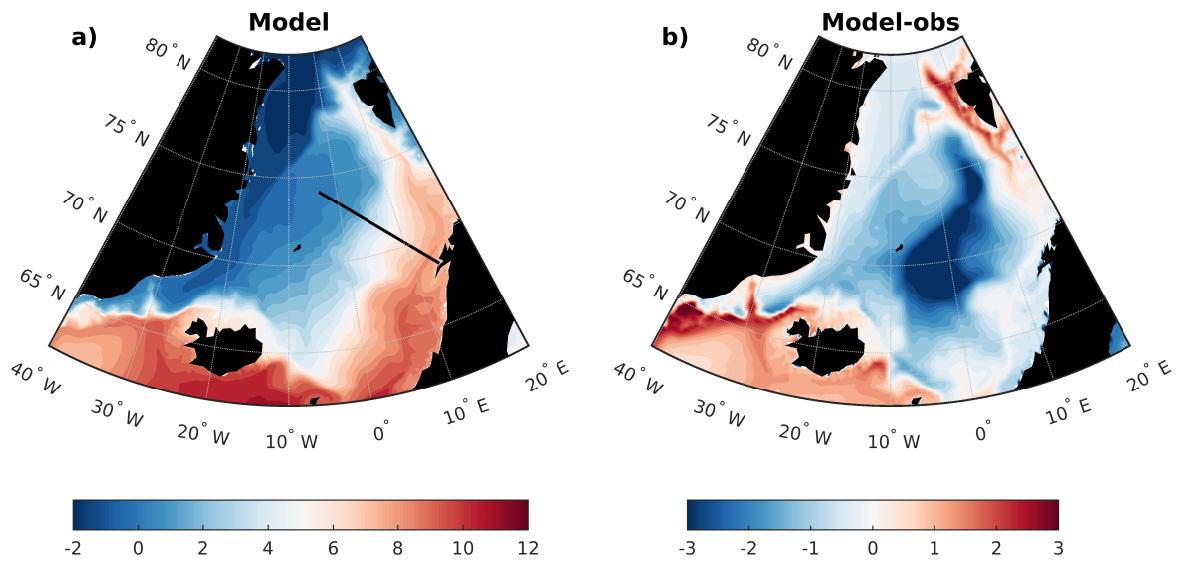
1001 FIG. 1. Bathymetry of the Nordic Seas (m). The main straits allowing exchanges with the Atlantic and the
 1002 Arctic are indicated: DS (Denmark Strait), IFR (Iceland Faroe Ridge), BSO (Barents Sea opening) and FS (Fram
 1003 Strait), as well as the main seas (Greenland, Iceland, Norwegian seas), deep ocean ridges (Knipovich, Mohn
 1004 and Jan Mayen), and the two deep basins of the Norwegian Sea (Lofoten Basin and Norwegian Basin). The
 1005 bathymetric field is taken from the GC3 1/12° model. The main currents carrying Atlantic water are outlined
 1006 in red (Norwegian Atlantic Slope Current, Norwegian Atlantic Front Current, West Spitzbergen Current). The
 1007 East Greenland Current, carrying Arctic water, is outlined in blue. The current paths are based on Taburet et al.
 1008 (2019).



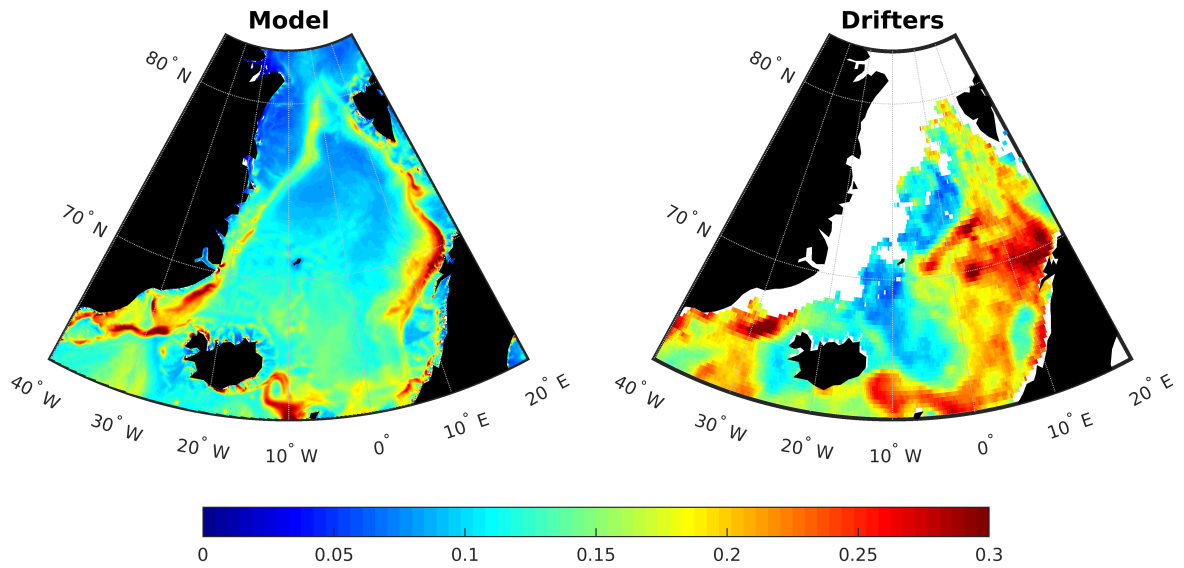
1009 FIG. 2. Ice concentration in the coupled model, averaged over 30 years in March (left) and September (right).
 1010 Grey contours indicate ice concentrations of 0.15 and 0.85. The red contours represent concentrations of 0.15
 1011 and 0.85 in NSIDC satellite observations for the same months, averaged over the 1991-2010 period.



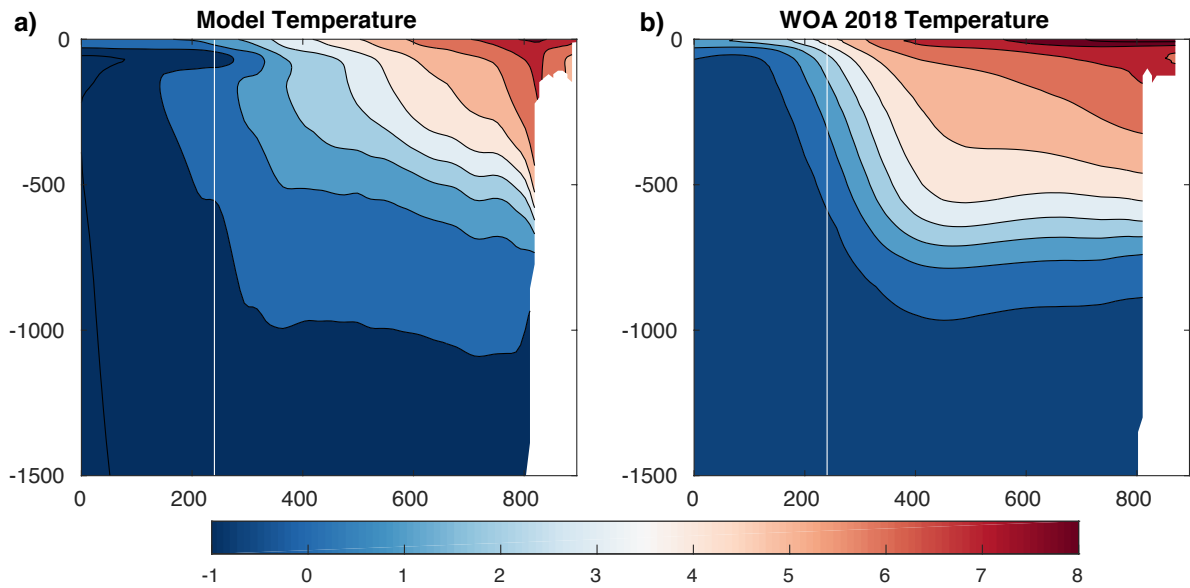
1012 FIG. 3. Ice area in the region 45°W to 20°E and 65°N to 80°N, monthly (thin lines) and annual averages (thick
 1013 line). a: observations. b: coupled model.



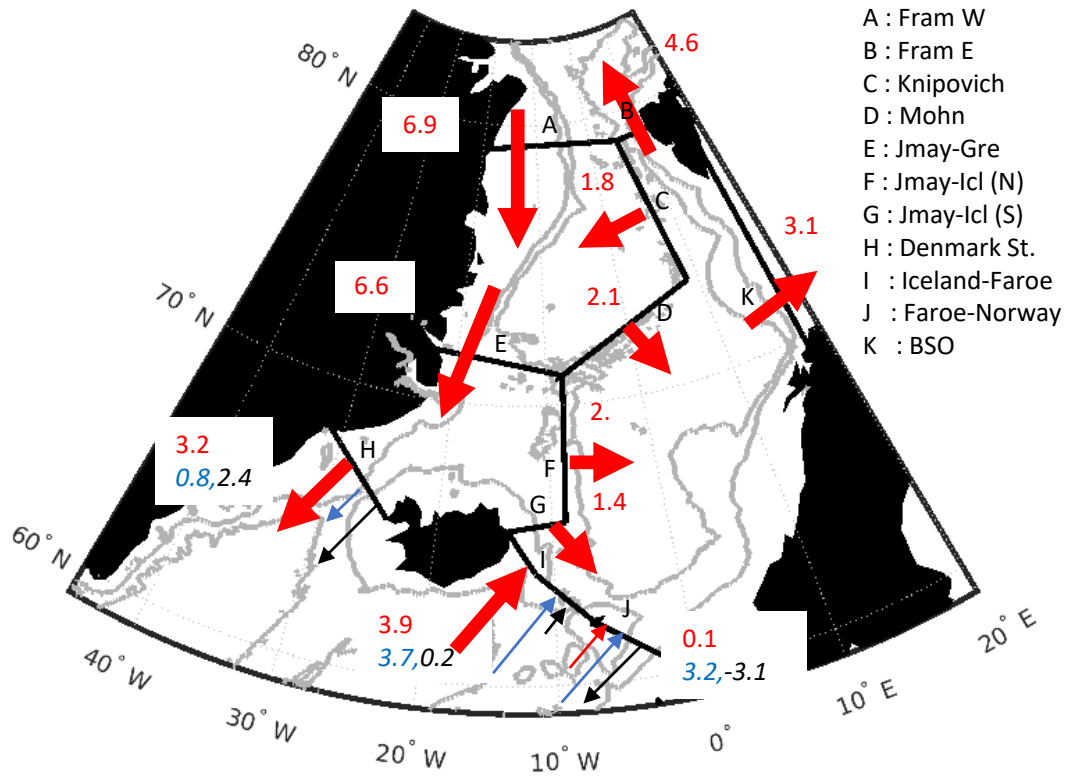
1014 FIG. 4. a: Sea surface temperature ($^{\circ}\text{C}$) averaged over 20 years in the coupled model. The black line is the
 1015 path of the Gimsøy section, used for Fig.6. b: difference between model SST and observed SST (averaged over
 1016 years 1991-2010).



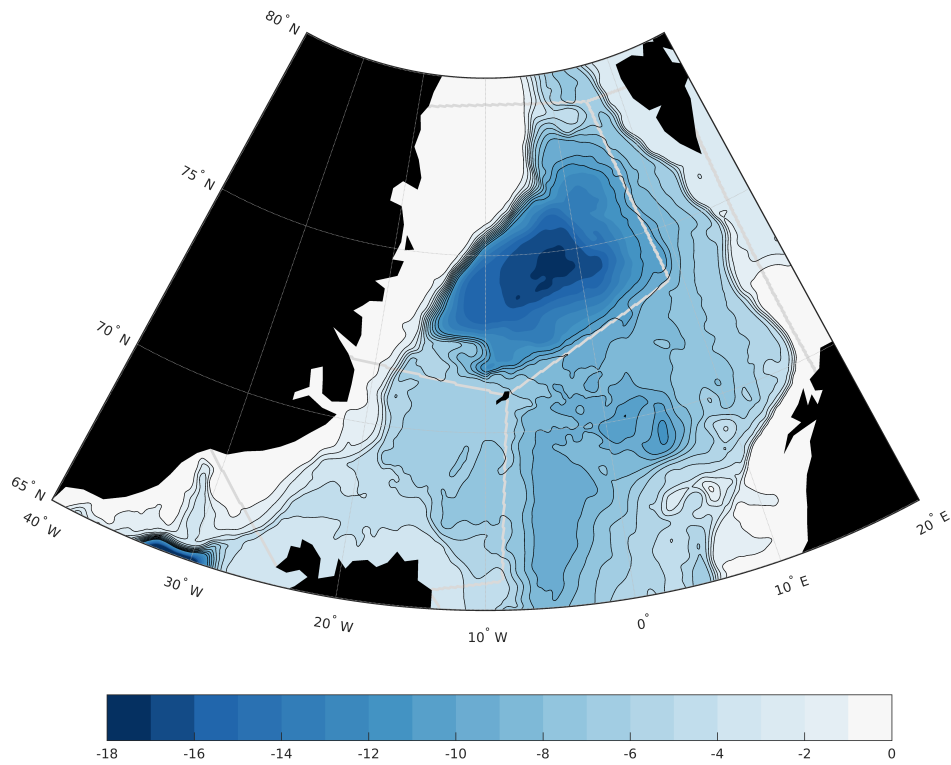
1017 FIG. 5. Left: rms surface velocity (m/s) from the GC3 coupled model. Right: rms surface velocity from a
1018 climatology of surface drifters (Laurindo et al. 2017).



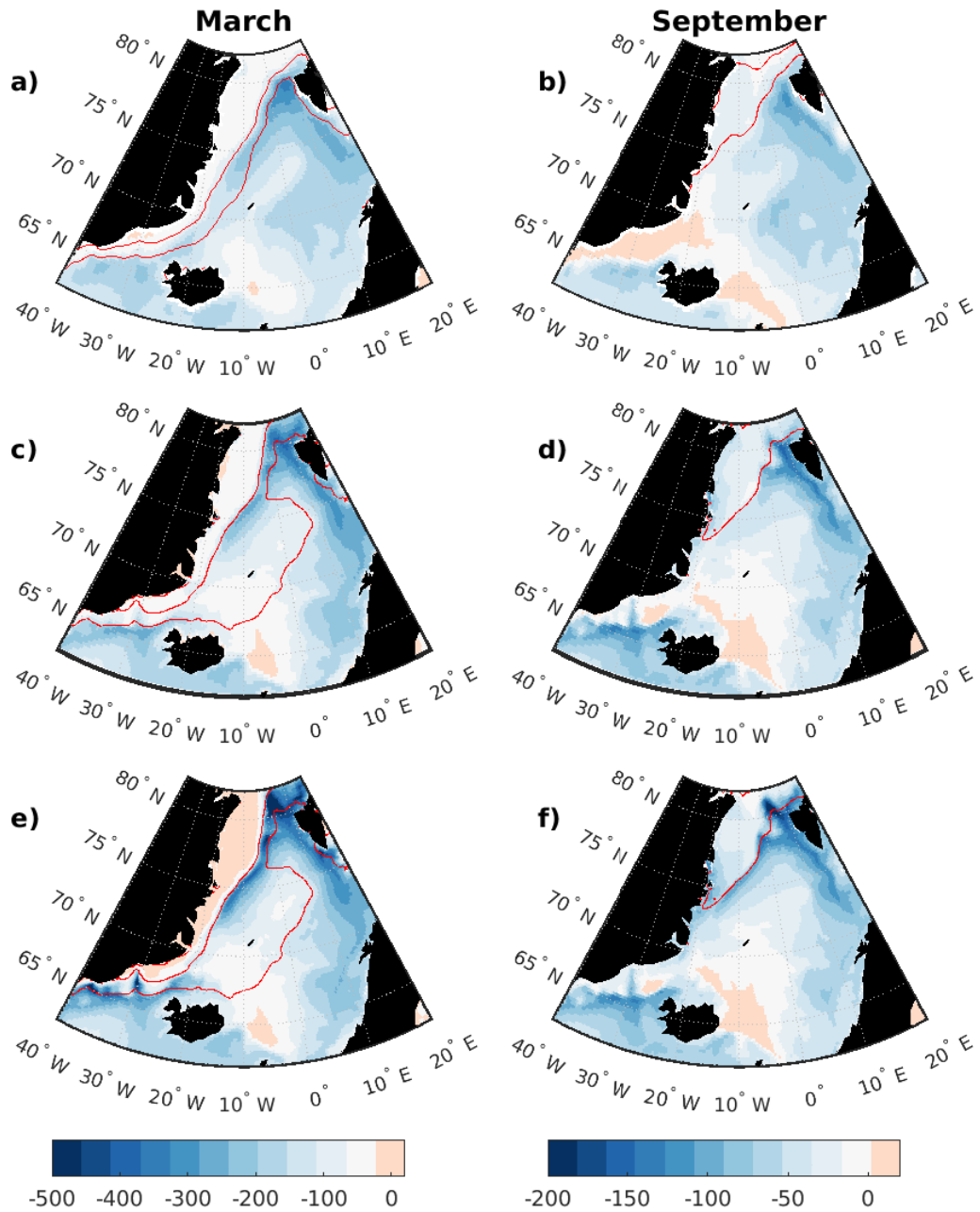
1019 FIG. 6. Climatological temperature ($^{\circ}\text{C}$) for the month of June along the Gimsøy section, indicated on the map
 1020 in Fig. 4a. a: GC3 model monthly mean, averaged over 30 years. b: monthly climatology from observations,
 1021 World Ocean Atlas 2018 (Locarnini et al. 2018). The white line indicates the top of Mohn Ridge.



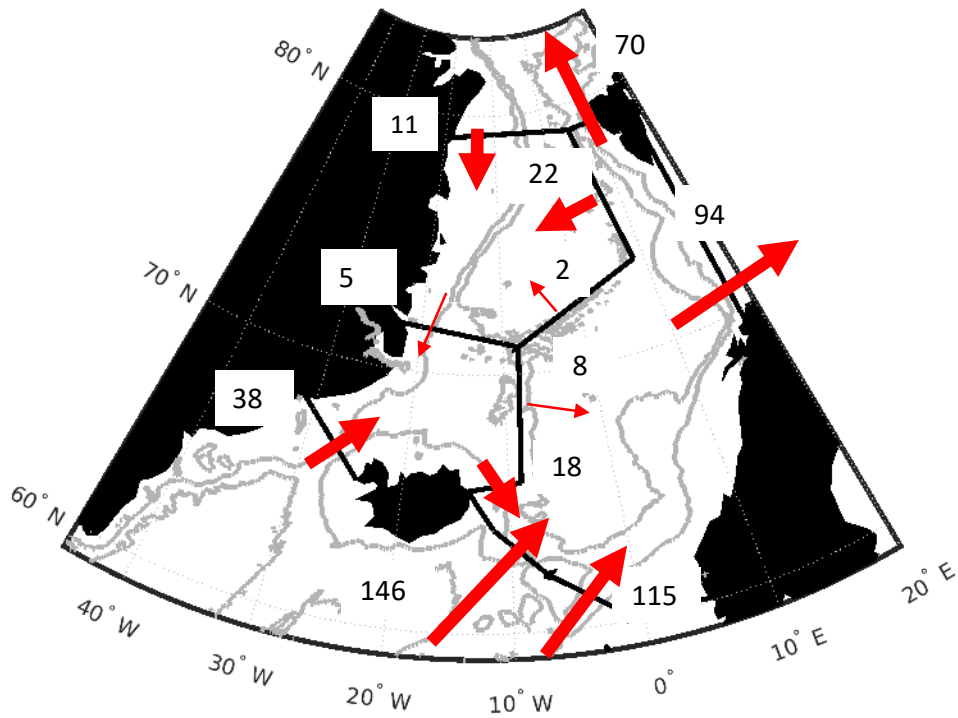
1022 FIG. 7. Mass balance of the Nordic Seas in the coupled model. Red arrows (red numbers) represent the depth-
 1023 integrated ocean mass flux (Sv) across the sections outlined in black. Short names are indicated for the sections;
 1024 they are used in the tables and explained in the text (e.g, "BSO" for Barents Sea Opening). For the southern
 1025 sections, the two additional numbers (blue and black) indicate the transport associated with mean densities lower
 1026 and higher than $\sigma_0 = 27.8$, respectively. The sign convention is such that a positive number is a contribution in
 1027 the same direction as the total indicated by the red arrow. Thin blue and black arrows indicate the direction of
 1028 these light inflows and dense overflows. The grey contours represent the 500 m and 2000 m isobaths.



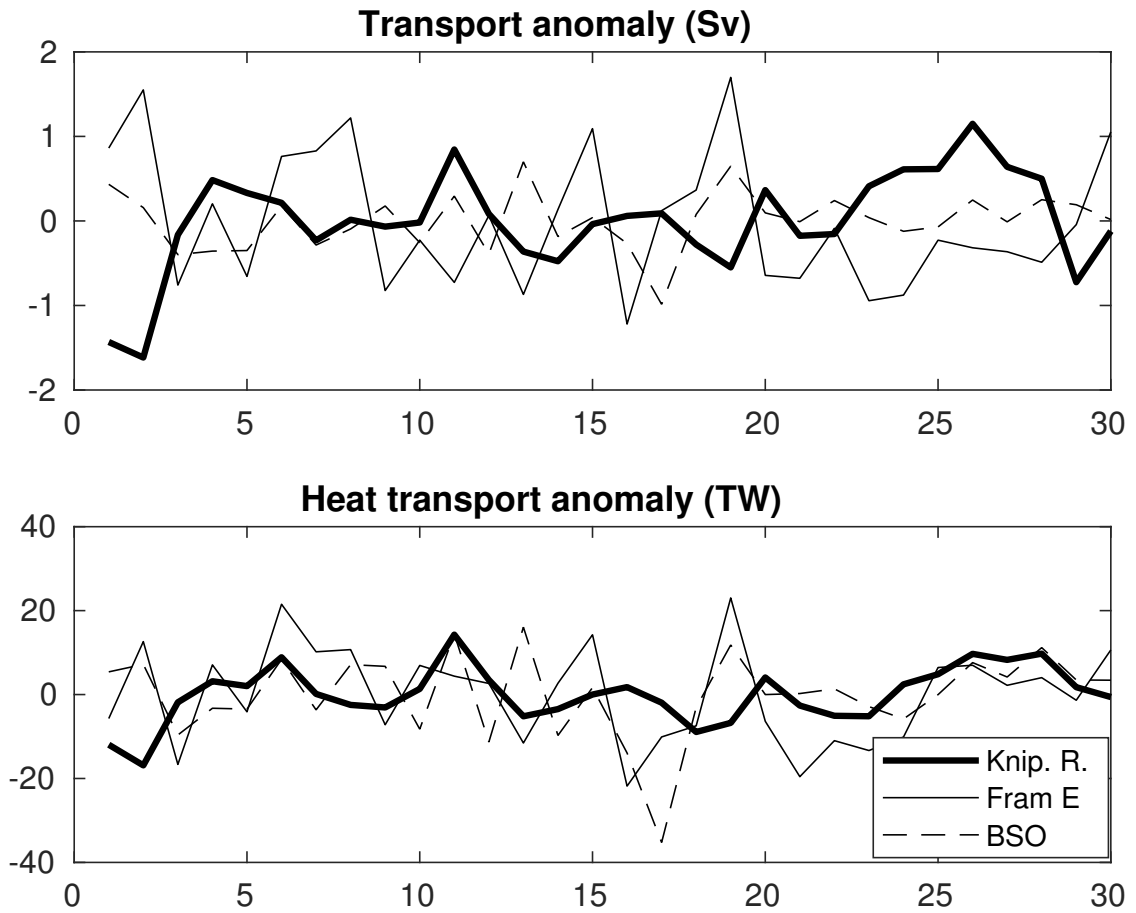
1029 FIG. 8. Barotropic streamfunction (Sv) in the coupled model, averaged over 30 years. The sections delimiting
 1030 the regions of Fig. 7 are indicated in grey. Only the contours from -1 Sv to -11 Sv are outlined in black, to better
 1031 show the transports entering and exiting the Greenland gyre, while keeping the readability of the figure.



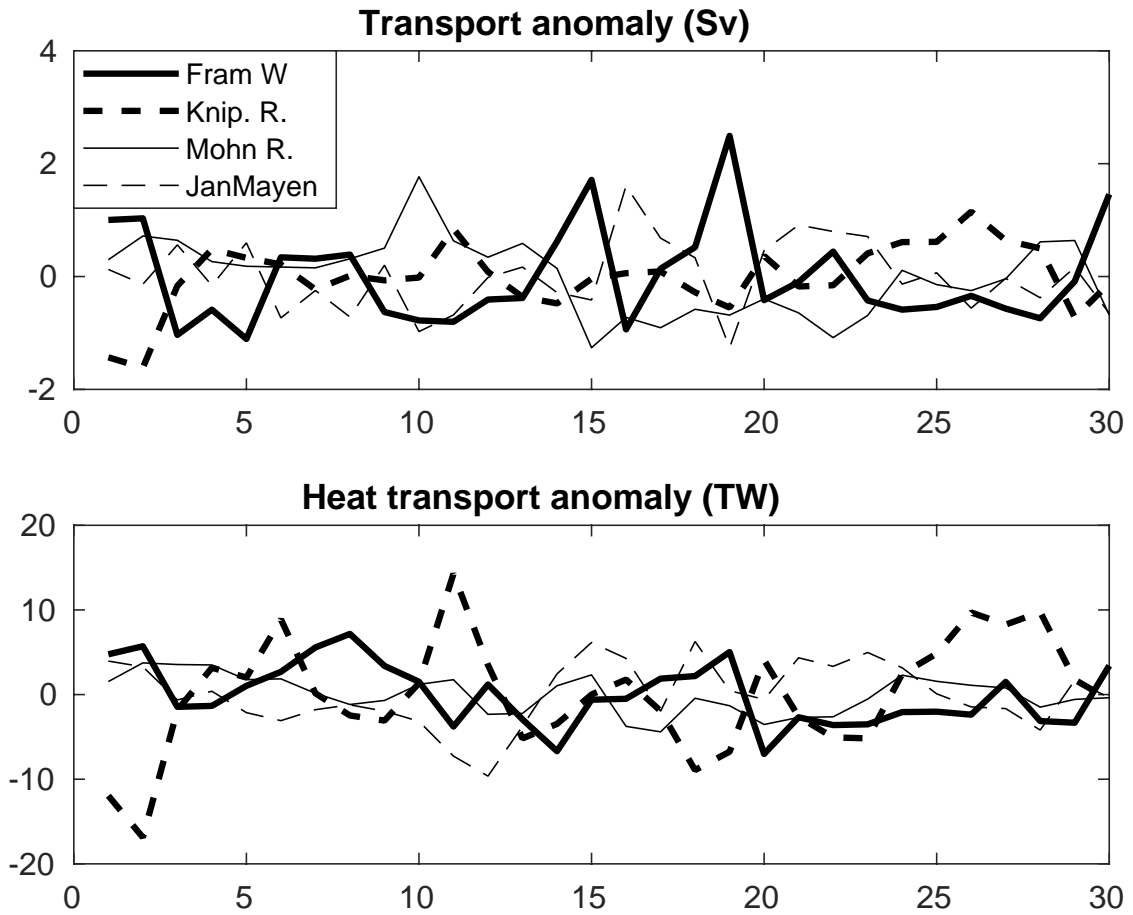
1032 FIG. 9. Surface heat flux climatologies for March (left panels) and September (right panels), in $W.m^{-2}$, with
 1033 the limits of the Marginal sea Ice Zone (MIZ) overlaid in red (concentration 0.15 and 0.85). a,b: heat flux at
 1034 the atmospheric lower boundary from ERA5 (averaged over years 2001-2010) and sea ice from NSIDC data . c,
 1035 d: heat flux at the atmospheric model lower boundary, with the modelled MIZ overlaid. e, f: ocean surface
 1036 heat flux and modelled MIZ. Note the different color scales for March and September.



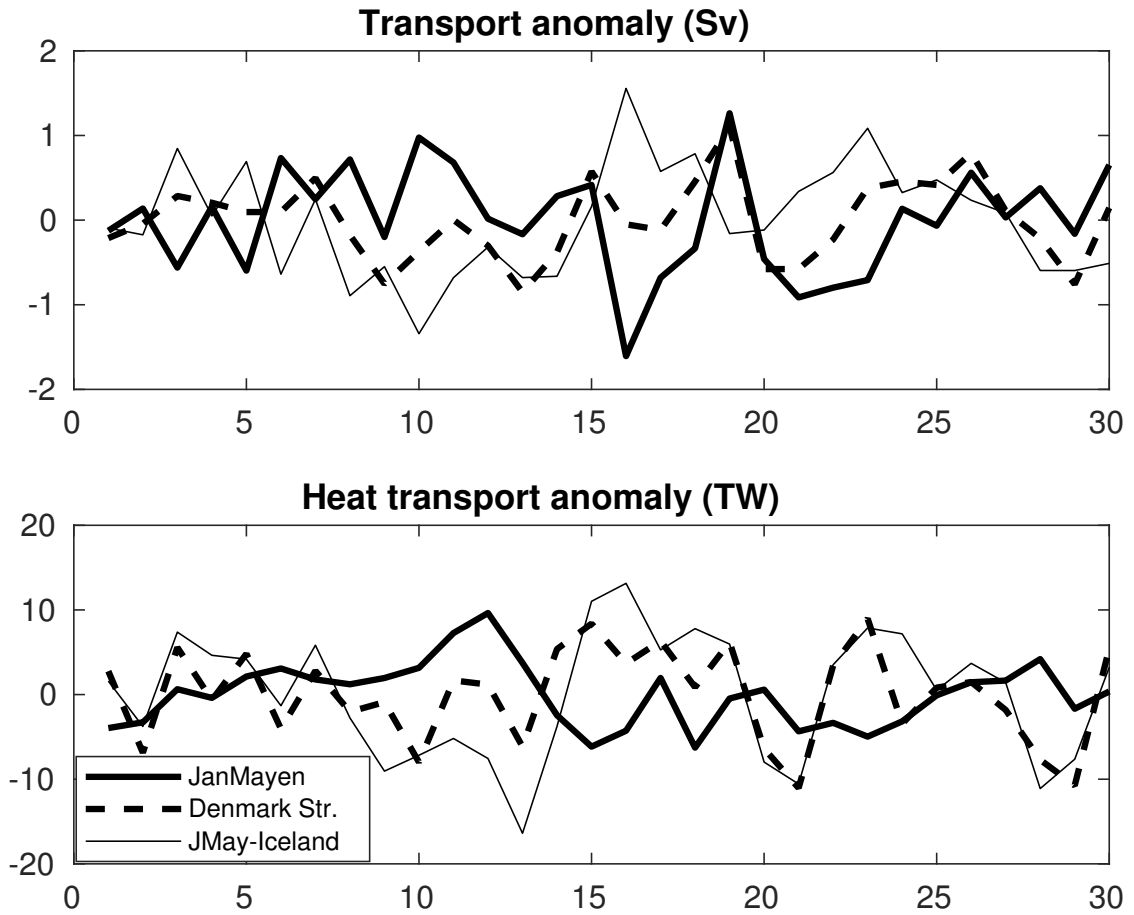
1037 FIG. 10. Heat balance of the Nordic Seas in the coupled model. Red arrows represent the heat flux referenced
 1038 to 0°C, in units of TW, across the sections outlined in black. Values have been rounded relative to the numbers
 1039 in Table.2 for readability. In the Greenland Sea and in the Iceland Sea the total convergence of heat, 30 TW and
 1040 16 TW respectively, balance the cooling at the ocean surface within less than 1 TW. In the Norwegian Sea, the
 1041 heat convergence of 99 TW differs from the surface heat loss (94 TW), generating a warming of 5 TW. The grey
 1042 contours represent the 500 m and 2000 m isobaths.



1043 FIG. 11. Interannual anomalies of volume and heat transport across the three sections where warm water exits
 1044 the Norwegian Sea: Barents Sea opening (BSO), Eastern part of Fram Strait (Fram E) and flow over Knipovich
 1045 Ridge (Knip. R). All transports are counted positively in the sense of an exit from the Norwegian Sea. The time
 1046 axis is in model years.



1047 FIG. 12. Interannual anomalies of volume and heat transport across the four sections enclosing the Greenland
 1048 Sea: Western part of Fram Strait (Fram W), flow over Knipovich Ridge (Knip. R) and Mohn Ridge (Mohn R.),
 1049 and between Greenland and the island of Jan Mayen. The time axis is in model years.



1050 FIG. 13. Interannual anomalies of volume and heat transport across the sections enclosing the Iceland Sea:
 1051 Denmark Strait, flow between Greenland and Jan mayen (JanMayen) and flow between Jan Mayen and Iceland
 1052 (JMay-Iceland). The time axis is in model years.